AFRL-AFOSR-VA-TR-2021-0052

A NEW GENERATION OF MODELS FOR RADAR TARGETS

Semyon Tsynkov
NORTH CAROLINA STATE UNIVERSITY
2601 WOLF VILLAGE WAY
RALEIGH, NC, 27607
USA

06/17/2021
Final Technical Report

Air Force Research Laboratory
Air Force Office of Scientific Research
Arlington, Virginia 22203
Air Force Materiel Command

REPORT DOCUMENTATION PAGE

Form Approved
OMB No. 0704-0188

1. REPORT DATE *(DD-MM-YYYY)*	**2. REPORT TYPE**	**3. DATES COVERED** *(From - To)*
17-06-2021	Final	01 Jul 2017 - 31 Dec 2020

4. TITLE AND SUBTITLE
A NEW GENERATION OF MODELS FOR RADAR TARGETS

5a. CONTRACT NUMBER

5b. GRANT NUMBER
FA9550-17-1-0230

5c. PROGRAM ELEMENT NUMBER
61102F

6. AUTHOR(S)
Semyon Tsynkov

5d. PROJECT NUMBER

5e. TASK NUMBER

5f. WORK UNIT NUMBER

7. PERFORMING ORGANIZATION NAME(S) AND ADDRESS(ES)
NORTH CAROLINA STATE UNIVERSITY
2601 WOLF VILLAGE WAY
RALEIGH, NC 27607
USA

8. PERFORMING ORGANIZATION REPORT NUMBER

9. SPONSORING/MONITORING AGENCY NAME(S) AND ADDRESS(ES)
AF Office of Scientific Research
875 N. Randolph St. Room 3112
Arlington, VA 22203

10. SPONSOR/MONITOR'S ACRONYM(S)
AFRL/AFOSR RTB1

11. SPONSOR/MONITOR'S REPORT NUMBER(S)
AFRL-AFOSR-VA-TR-2021-0052

12. DISTRIBUTION/AVAILABILITY STATEMENT
A Distribution Unlimited: PB Public Release

13. SUPPLEMENTARY NOTES

14. ABSTRACT
We have developed and analyzed a family of both deterministic and stochastic models for synthetic aperture radar targets. The models allow one to linearize the scattering about the target without having to assume that it is weak, account for anisotropy (and separately analyze the anisotropy of the propagation medium), non-flat topography, temporal dispersion, speckle, and texture. We have built algorithms for SAR reconstruction that include the differential Faraday rotation and distinguish between the instantaneous and delayed targets. We have provided a comprehensive quantitative analysis of SAR interferometry. The original objectives of the project have been met. The results have been published in scholarly Journals and presented and the various national and international Conferences.

15. SUBJECT TERMS

16. SECURITY CLASSIFICATION OF:			**17. LIMITATION OF ABSTRACT**	**18. NUMBER OF PAGES**	**19a. NAME OF RESPONSIBLE PERSON**
a. REPORT	**b. ABSTRACT**	**c. THIS PAGE**			ARJE NACHMAN
U	U	U	UU	40	**19b. TELEPHONE NUMBER** *(Include area code)* 426-8427

FINAL PERFORMANCE REPORT

To: technicalreports@afosr.af.mil
Subject: Final Performance Report to Dr. Arje Nachman

Contract/Grant Title: **A new generation of models for radar targets**
Contract/Grant #: FA9550-17-1-0230
Overall Performance Period: 01 July 2017 – 31 March 2021 (includes a CoViD-19 NCE from 01 January 2021 through 31 March 2021)

The project aims at addressing a number of important issues that arise in quantitative modeling of targets for synthetic aperture radars (SAR), including spaceborne radars that perform imaging through the Earth's ionosphere.

Conventional deterministic models for radar targets interpret the SAR observable as a variation of the local refractive index against constant background. To enable efficient inversion, one also assumes that this variation is small so that the resulting scattering is weak and can be linearized by applying the first Born approximation. From the standpoint of physics, this approach is deficient. This is easy to see because already in the most basic case of a flat uniform target, it does not allow for any backscattering and always yields a specular reflection. Moreover, it is not compatible with the common hypothesis that the scattering occurs only at the surface of the target. The new type of models we have constructed overcome these deficiencies by keeping the scattering linear yet not necessarily weak. These models involve a dielectric half-space with variable permittivity and interpret the SAR observable as amplitude of the resonant Bragg harmonic in its local Fourier spectrum.

However, the deterministic models alone are not capable (yet) of adequately representing the important phenomenon of speckle, which is due to the coherent mechanism of SAR imaging. A radar image with speckle inherits some of the small-scale roughness and thus looks "bumpy" (i.e., shows strong and rapid variations of the amplitude and phase) while the actual parameters of interest vary gradually on a longer scale and are smooth. To account for speckle, one usually employs stochastic models that are inherently phenomenological. These models take the reflectivity function as a random field that generates speckled images like those observed in practice. Those reflectivity functions, however, may not always be related to the physical properties of the target; they are typically chosen according to the desired/convenient statistical properties.

Speckle significantly hampers our ability to resolve the small-scale or low-contrast variations of the average reflectivity of the radar scene. It is always present in SAR images and needs to be accounted for when analyzing SAR reconstruction for various types of targets.

Of particular importance in practice are targets that exhibit temporal dispersion, i.e., scattering with time delay. The delay may be due to either the material composition of the target or its shape (cavities) or both. Specific characteristics of dispersion may provide useful information for target identification.

Speckle can obscure the delayed target response in SAR imaging. It further exacerbates the adverse effect of the range-delay ambiguity that mixes up a delayed response from a closer target with an instantaneous response from a more remote target. The range-delay ambiguity is a deterministic phenomenon though; it can be described and analyzed by allowing both the target reflectivity and image to depend not only on the spatial coordinates, but also on the response delay, and extending the conventional SAR ambiguity theory accordingly. The analysis of speckle, on the other hand, requires a stochastic approach.

Accomplishments during the first performance period (01 July 2017 – 30 June 2018):

Radar targets often exhibit material anisotropy, which affects the polarization of the scattered signal relative to that of the impinging signal. The polarimetric SAR instruments (PolSAR) take images in four channels that represent the four possible combinations of two linear polarizations (horizontal and vertical) of the impinging and scattered waves. There are, however, other physical phenomena that may also have an effect on polarization. First and foremost, the propagation of the linearly polarized electromagnetic waves through the Earth's ionosphere is accompanied by Faraday rotation (FR), which is a slow rotation of the polarization plane of the wave that accompanies its propagation. The rotation angle is determined by the magnetic field of the Earth, total electron content, signal frequency, and propagation direction. The mechanism of Faraday rotation is due to double circular refraction caused by a special form of anisotropy, known as gyrotropy, that characterizes the magnetized ionospheric plasma. FR may lead to distortions of images taken by spaceborne polarimetric SAR. Therefore, accurate quantification of those distortions and the development of means for their mitigation are very important for the subsequent analysis of anisotropies that characterize the SAR targets and scattering about those targets.

We have shown that a key mechanism of FR-induced distortions in PolSAR images is the variation of the FR angle within the bandwidth of the interrogating radar signals (chirps). We call this effect the differential Faraday rotation (dFR). It has not been previously accounted for in the context of SAR imaging. To compensate for dFR, we have proposed a special matched filter that we refer to as the polarimetric matched filter (PMF). The PMF helps correct the FR-induced distortions and provides a provably superior SAR performance compared to the case of the traditional polarimetric SAR signal processing.

The mitigation of the effect of dFR on PolSAR images involves a rotation matrix, where the rotation angle is the FR angle. We have analyzed the conditions where neither the signal frequency nor the angle between the propagation direction and the magnetic field can be considered constant. In other words, a rotation matrix based on the main look direction and central carrier frequency would have a significant mismatch with the received signal in fast or slow time. We have obtained estimates for the resulting polarimetric distortions and their effect on applications such as the instrument calibration in space and the measurement of the aboveground biomass [1-3].

Another key phenomenon of interest is temporal dispersion of radar targets, i.e., their delayed response, which may be caused by the material composition or concave shape of the target, or both. The specific characteristics of dispersion may provide useful information for target identification. Yet the delayed target response in SAR is obscured by the range-delay ambiguity and

speckle. If the standard SAR ambiguity theory is extended by allowing both the target reflectivity and the image to depend not only on the spatial coordinates, but also on the response delay, then the range-delay ambiguity can be described and analyzed, but the speckle will remain unaccounted for. Since statistical approach is usually needed to describe the speckle, we have constructed a model for delayed scatterers by modifying the random function that describes a homogeneous distributed scatterer. Our approach helps us obtain a stochastic imaging operator that maps the deterministic parameters of the target onto statistical moments of the SAR image.

Accomplishments during the second performance period (01 July 2018 – 30 June 2019):

We have developed a family of stochastic models for instantaneous distributed scatterers and delayed localized scatterers in speckle. Our models allow one to build the stochastic imaging operators and obtain the required relations between the deterministic parameters of the target and statistical moments of the corresponding SAR image. Under the specific model assumptions, the expectations and correlations of the image are derived analytically. Then, the problem of reconstruction of the coordinate-delay reflectivity function reduces to that of discrimination between the instantaneous and delayed scatterers. The latter can be addressed using a maximum likelihood-based methodology. The performance of our target classification procedure has been demonstrated using Monte-Carlo simulations [5].

Yet in the presence of speckle, the weak and slow variations along the ambiguity directions in the SAR image can be nearly undetectable (ambiguity directions are the space-time directions associated with the range-delay ambiguity). This means that the discrimination between the instantaneous and delayed targets may not be sufficiently robust. We have shown that increasing the sample size, i.e., the amount of data supplied to the discrimination functional, increases the robustness of target classification as either instantaneous or delayed. In addition, we have developed an approach to quantifying the reliability of target classification by means of confidence levels. Confidence levels have been introduced for the enhanced discriminating functional and the performance of the resulting discrimination procedure was demonstrated for different system and target parameters. Confidence levels are crucial for SAR applications because in practice, it is often not possible to obtain additional images of the same target under similar conditions [5-7].

Accomplishments during the third performance period (01 July 2019 – 30 June 2020):

Temporal delay in electromagnetic scattering is a manifestation of the complex geometry and/or internal structure of a radar target. The coordinate-delay SAR (cdSAR) images provide a convenient mathematical model for the detection and characterization of such targets. We build the cdSAR images by adding a delay term to the standard SAR matched filter. In order to apply this approach to the case of extended targets in speckle, we sample a cdSAR image at several coordinate-delay "points" in the vicinity of the scatterer location. The instantaneous and delayed targets are subsequently discriminated from one another using the autocorrelation analysis of this sample and the notions of maxim likelihood and confidence levels [5-7].

Because of the statistical representation of speckle, misclassification errors are inevitable. Hence, prediction of the error rate as a function of system and target parameters becomes an important problem. The error rate can be calculated directly using the ensembles of data generated by Monte-Carlo simulations. However, this approach is computationally demanding because of its slow convergence. To simplify the prediction of the error rate, we proposed to use the statistical divergence measures, namely, the Hellinger distance and Kullback-Leibler divergence. These divergence measures are obtained from the theoretical models of reflectivity of extended targets that we want to analyze. For a certain class of target models, we have empirically established a linear relation between the misclassification rate and Hellinger distance. This relation allows us to make predictions of the error rate without performing the Monte-Carlo simulations [8].

We have also applied a convolutional neural network (CNN) to the problem of discrimination between the instantaneous and delayed targets in SAR images. The misclassification rate, which is always nonzero due to the stochasticity of the radar data, depends on the parameters of the radar system, imaging scene, and observation settings. A trained CNN demonstrates the discrimination quality that is at least as good as the one of the previously developed classifier based on the principle of maximum likelihood [9].

Perhaps the most common stochastic model for the reflectivity of both radar targets and the surrounding background (clutter) is a Gaussian delta-correlated process, or white noise. For dispersive targets, the reflectivity autocorrelation function also depends on the delay time. The corresponding cdSAR image presents the reflectivity as a function of the coordinates and delay and is accompanied by speckle. Speckle hampers our ability to discriminate between different types of radar targets based on a single cdSAR image, even though the statistical properties of cdSAR images are different for delayed and instantaneous targets. When texture is introduced into the background by means of a non-zero correlation length (so that the stochastic process that models the target reflectivity is no longer delta-correlated), the resulting background inhomogeneities can also be misclassified as targets. We have analyzed the options to simulate and detect the delayed targets superimposed on a correlated, i.e., textured, background [10].

Standard SAR produces two-dimensional maps of target reflectivity. The lack of a third dimension is related to the geometry of imaging with an aperture that is a segment of a straight line. In this case, the actual three-dimensional reflectivity function is collapsed across the slant plane. Yet the resulting two-dimensional images can adequately represent the geometric features of a scatterer that is flat or nearly flat, such as a small patch of the Earth's surface. Interferometric SAR (InSAR) is a first step toward obtaining the third coordinate. For a scatterer that is two-dimensional but not flat, InSAR can supplement regular SAR by providing the elevation map. This is achieved by combining the complex-valued SAR images obtained from two apertures that correspond to two different slant planes and analyzing the phase difference between them.

Interferometric tasks require centimeter-level accuracy, which is remarkable given that for spaceborne radar systems, the distance between the radar and its target is many hundreds of kilometers, i.e., about a hundred million times larger than the changes to be detected. The required sensitivity is enabled by comparing the complex phases of two images, which allows one to detect the differences in signal path length as small as a fraction of the radar wavelength. However, the interaction of radar signals with the target, as well as the lack of precision in antenna position

and other disturbances, generate ambiguities of the image phase that are orders of magnitude larger than the effect of interest.

Yet the common exposition of radar interferometry in the literature often skips the various important details related to ambiguities of interferometric measurements. This may lead to unrealistic requirements for the accuracy of determining the parameters of imaging geometry, unachievable precision of image co-registration, etc. To address these deficiencies, we have thoroughly analyzed the problem of interferometric height reconstruction and provided a careful and detailed account of all the assumptions and requirements to the imaging geometry and data processing needed for a successful extraction of height information from the radar data. In doing so, we employed two scattering models for radar targets: an isolated point scatterer and delta-correlated extended scatterer and highlighted the similarities and differences between them [11].

The need to accommodate the essentially three-dimensional targets, such as the terrain covered with vegetation, prompted the development of more involved technologies. Polarimetric radar interferometry (PolInSAR) can extract some parameters of the three-dimensional scatterer using a single pair of apertures. For example, by exploiting the difference in reflectivities and correlation properties between the ground and vegetation for different polarizations, PolInSAR can retrieve multiple geometrical parameters of the vegetation layer covering the Earth's surface, including the vegetation height and underlying ground topography.

Accomplishments during the fourth performance period (01 July 2021 – 31 December 2020 and a CoViD-19 NCE from 1 January 2021 through 31 March 2021):

A key difficulty encountered with PolInSAR is that any cross-talk between the polarimetric channels of a radar system violates the PolInSAR assumptions and reduces the reconstruction accuracy. One source of such cross-talk for spaceborne SAR is the differential Faraday rotation that we studied in [1]. It becomes quite noticeable for the radars operating on lower frequencies (e.g., P-band) that offer a better ground and foliage penetrating capability. We have therefore derived an accurate estimate of the effect of dFR on PolInSAR reconstruction for the case where the polarimetric matched filter (PMF mitigation) has not been used. We employed a well-known PolInSAR reflectivity model called random volume over ground (RVoG) and interpreted the distortions due to dFR as if they were caused by noise. The resulting reconstruction errors provide a quantitative measure of the effect of dFR on PolInSAR performance [12].

Convolutional neural networks have shown promise in distinguishing between the instantaneous and dispersive radar targets [9]. It is therefore of keen interest to test the discrimination capacity of CNNs for those imaging scenarios for which a classifier based on maximum likelihood (with confidence levels) may be more difficult to build. Going beyond the plain discrimination between the instantaneous and delayed targets, it would also be very useful if one can obtain resolution in the delay variable.

To address these goals, we have developed a capability to produce datasets of simulated coordinate-delay SAR images of targets with a certain class of reflectivity models that may or may not include the scattering delay. These images are three-dimensional, corresponding to two

spatial dimensions (range and cross-range, as in standard SAR) and, additionally, one delay variable. We can also simulate instantaneous textured background and noise with varying spatial characteristics and intensities. The overall objective is to locate the target on the image and characterize its scattering delay.

The previous publication on the subject [9] presented the results on two-dimensional images (no cross-range coordinate) with a fixed location of the target and no texture in the background. For this case, a maximum likelihood classifier has been implemented and used as a benchmark for the deep learning-based classifier.

A "You Only Look Once," or YOLO, type CNN model has been built for the analysis of 3D cdSAR images. It has shown the capacity to predict the coordinates and delay of a target with certain accuracy. However, similar predictions, although with a lesser accuracy, can be obtained from another YOLO model that uses zero-delay (2D) slices of 3D images. Physically, determining the scattering delay from the image data with no span in the delay direction should not be possible. The fact that this is happening points to an unintentional feature of the dataset that allows “leakage” of the 3D information into a 2D image.

From the standpoint of achieving our immediate goals, learning from this leaked information may be undesirable. We are therefore considering the “unlearning” strategies in order to evaluate the foregoing effect and, if possible, suppress this kind of learning. One approach is to add the “attention mechanism” to the 2D YOLO model to identify the areas in the 2D images that carry the delay information. This has been done successfully: certain attention masks clearly correlate with the location of the target. However, we still need to see how to control the classifier by means of manipulating these “interpretable” masks. Another possible way to achieve the unlearning is via using the "delay-noise" images, which are the 3D images where the delay information has been intentionally destroyed.

In a broader context, however, the capacity to recover the 3D information from 2D observations may obviously be beneficial. To that end, achieving the unlearning objective will hopefully help us understand the mechanism of leakage from 3D cdSAR images to their 2D slices so that one can subsequently exploit it to the advantage of the reconstruction task. It is possible that considering the fixed-delay slices instead of zero-delay slices of the 3D images may prove useful.

We are contemplating several additional publications on the subject of machine learning as it applies to the analysis of coordinate-delay SAR images:

- Extension of [9] to 3D. Main points: known location of the target and absence of texture allow for a straightforward construction of a maximum likelihood-based classifier. We need to reproduce in 3D the study of dependence of the classification quality on the parameters of the physical model: contrast, size of target, magnitude of delay, etc. A very important generalization is the capacity to quantify the delay rather than only distinguish between the delayed and instantaneous scattering.
- Target detection and delay quantification with the help of the currently available YOLO model: performance, sensitivity to parameters, etc.
- Treatment of 3D learning from 2D data as overfitting, with 2D unlearning playing the role of regularization.

Otherwise let us emphasize that, currently the physics-based deterministic models of radar targets that associate the scattering mechanisms of impinging signals with surface inhomogeneities on the short scale and phenomenological stochastic models that account for speckle in SAR images are built independently. In the long run, it would be desirable to bring these two types of models closer to one another. Ideally, one would like to develop a physics-based linear model of scattering about the surface of a target capable of representing both backscattering and speckle. Preferably, this model should also account for the possible scattering anisotropy, i.e., the dependence of target reflectivity on the viewing direction. The latter can, perhaps, be attributed to physical mechanisms via the directional dependence of Bragg resonances.

Altogether, all the research goals set forth the in the beginning of the project have been met. The results are summarized in the scholarly publications listed at the end of the report that include both journal and conference papers. Reference [12], which is still an unpublished manuscript, is attached with the report. In addition, the results have been presented at four AFOSR Electromagnetics Program Review Workshops: 2018, 2019, 2020, and 2021.

Personnel:

Prof. S. Tsynkov – PI, Dr. M. Gilman – Research Assistant Professor, Dr. J. Lagergren – Graduate Research Assistant (PhD Candidate).

Publications:

1. M. Gilman and S. Tsynkov, Differential Faraday rotation and polarimetric SAR, *SIAM Journal on Applied Mathematics,* 78, No. 3 (2018) pp. 1422-1449. https://doi.org/10.1137/17M114042X
2. M. Gilman and S. Tsynkov, Cross-channel Contamination of PolSAR Images due to Frequency Dependence of Faraday Rotation Angle, in Proceedings of the *2018 IEEE Conference on Antenna Measurements and Applications,* 3-6 September 2018, Västerås, Sweden (4 pp). https://doi.org/10.1109/CAMA.2018.8530603
3. M. Gilman, E. Smith, and S. Tsynkov, Polarimetry of homogeneous half-spaces, *Workshop on Symbolic-Numeric Methods for Differential Equations and Applications*, Courant Institute of Mathematical Sciences, NYU, 20 July 2018.
4. S. Tsynkov, Synthetic aperture imaging through a turbulent ionosphere, International Conference *Advances in Applied Mathematics,* Tel Aviv University, 18-20 December 2018, Tel Aviv, Israel https://stsynkov.math.ncsu.edu/Memorial_Conference/agenda.html
5. M. Gilman and S. Tsynkov, Detection of delayed target response in SAR, *Inverse Problems,* 35 (2019) 085005 (38pp). https://doi.org/10.1088/1361-6420/ab1c80
6. M. Gilman and S. Tsynkov, Stochastic Models in Coordinate-Delay Synthetic Aperture Radar Imaging, in Book of Abstracts, *The 14th International Conference on Mathemati-*

cal and Numerical Aspects of Wave Propagation (WAVES 2019), Vienna University of Technology, 25-30 August 2019, Vienna, Austria, pp. 330-331. https://doi.org/10.34726/waves2019
7. M. Gilman and S. Tsynkov, Statistical characterization of scattering delay in synthetic aperture radar imaging, *Inverse problems & Imaging,* 14, No. 3 (2020) pp. 511-533. https://www.aimsciences.org/article/doi/10.3934/ipi.2020024
8. M. Gilman and S. Tsynkov, Divergence Measures and Detection Performance for Dispersive Targets in SAR, *Radio Science,* 56, No. 1 (2021) pp. e2019RS007011. https://doi.org/10.1029/2019RS007011
9. J. Lagergren, K. Flores, M. Gilman, and S. Tsynkov, Deep learning approach to the detection of scattering delay in radar images, *Journal of Statistical Theory and Practice,* 15, No. 1 (2021) Paper No. 14. https://doi.org/10.1007/s42519-020-00149-w
10. M. Gilman and S. Tsynkov, Simulation of dispersive targets in SAR with textured background, *SIAM Conference on Imaging Science (IS20),* 6-17 July 2020, Happening Virtually (Originally scheduled in Toronto, Ontario, Canada). https://meetings.siam.org/sess/dsp_talk.cfm?p=105370
11. M. Gilman and S. Tsynkov, A mathematical perspective on radar interferometry, to appear in *Inverse problems & Imaging.*
12. M. Gilman and S. Tsynkov, Polarimetric radar interferometry in the presence of differential Faraday rotation, *in preparation.*
13. M. Gilman and S. Tsynkov, Synthetic aperture radar (SAR) imaging through a turbulent ionosphere, AMS Virtual Joint Mathematics Meetings (JMM), January 6-9, 2021. https://www.jointmathematicsmeetings.org/amsmtgs/2247_abstracts/1163-86-493.pdf
14. M. Gilman and S. Tsynkov, A mathematical perspective on radar interferometry, AMS 2021 Spring Southeastern Sectional Meeting, virtual delivery, March 13-14, 2021. http://www.ams.org/amsmtgs/2287_abstracts/1164-78-31.pdf

Changes in research objectives, if any: None.

Change in AFOSR program manager, if any: None.

Extensions granted or milestones slipped, if any: a CoViD-19 NCE from 01 January 2021 to 31 March 2021.

Polarimetric radar interferometry in the presence of differential Faraday rotation*

Mikhail Gilman† Semyon Tsynkov‡

June 15, 2021

Contents

*Work supported by US AFOSR, grant # FA9550-17-1-0230.

†Department of Mathematics, North Carolina State University, Raleigh, NC, 27695, USA. E-mail: mgilman@ncsu.edu, URL: https://mgilman.math.ncsu.edu.

‡Department of Mathematics, North Carolina State University, Raleigh, NC, 27695, USA. E-mail: tsynkov@math.ncsu.edu, URL: https://stsynkov.math.ncsu.edu.

1 Introduction

The standard synthetic aperture radar (SAR) imaging produces two-dimensional maps of target reflectivity. The lack of a third dimension is related to the geometry of imaging with an aperture that typically is a segment of a straight line (see, e.g., [1, 2, 3]). When the reflectivity function of a target is three-dimensional, the standard SAR collapses this function across the slant plane, which is a plane passing through the target and the aperture. Yet, two-dimensional images yield a satisfactory representation of geometric features of a scatterer that is flat or nearly flat, such as a small patch of the Earth surface.

Interferometric SAR, or InSAR, is a first step towards obtaining the third coordinate in the radar image. For a scatterer that is two-dimensional but not flat, InSAR can supplement SAR by providing an elevation map [1, 2]. This is achieved by combining the complex-valued SAR images obtained from two apertures corresponding to different slant planes and analyzing the phase difference between these images. Most often, InSAR involves apertures that are parallel or almost parallel, yielding two slightly different incident angles. Such technology has been used to build global digital elevation maps (DEMs) in satellite-based radar missions such as SRTM [4] and TanDEM-X [5]. A mathematical perspective on SAR interferometry is presented in our recent paper [6].

The need to extend radar remote sensing to essentially three-dimensional targets, such as vegetation-covered terrain, has brought about more involved technologies. In some experiments, more than 10 apertures are combined [7] to resolve details in the direction across the slant plane. Such setups are rare and expensive. By contrast, polarimetric radar interferometry, or PolInSAR [8, 9, 10], can extract some parameters of three-dimensional scatterer geometry using a single pair of apertures. For example, by exploiting the difference in reflectivities and correlation properties between ground and vegetation at different polarizations, PolInSAR can retrieve multiple geometrical parameters of vegetation layer covering the Earth surface, including vegetation height and the underlying ground topography.

Any cross-talk between the polarimetric channels of the radar system violates the PolInSAR assumptions and, as a result, deteriorates its reconstruction accuracy. The differential Faraday rotation (dFR) in the Earth's ionosphere, see [11, 12], has been shown to be a potential source of such cross-talk for satellite-based radar systems. This effect is very small for the previously mentioned C/X-band SRTM and TanDEM-X missions because of their relatively high radar frequencies. However, the need for ground and foliage penetration requires radar systems with much lower frequencies. For example, the central frequency of the future BIOMASS radar [13, 14] is dozens of times lower than those used in the past global radar DEM missions. It then makes sense to obtain quantitative estimates of this effect for currently active and future missions.

The Faraday rotation (FR) is a rotation of the polarization plane of a linearly polarized electromagnetic signal; this effect is well known in the community associated with satellite-based radar imaging (see, e.g., [15, 16, 17, 18, 19, 20, 21, 22]). In fact, FR is sometimes used as a tool for obtaining the ionospheric total electron content (TEC), which is the electron concentration integrated along the elevation. In turn, dFR is due to the dependence of the FR angle on frequency; hence, for a pulsed radar having a certain bandwidth, dFR will always be present. A series of publications describing the dFR effect has recently appeared [11, 23, 12, 24], and a mitigation method for this effect, called the polarimetric matched filter

(PMF), has been proposed in [11]. To the best of the author's knowledge, the effect of dFR on PolInSAR reconstruction has not been studied before.

In this work we derive an estimate of the effect of dFR on PolInSAR reconstruction for the case where the PMF mitigation is not used. We build a simplified PolInSAR problem statement that uses only two polarizations but still manifests the most significant features of a popular PolInSAR reflectivity model called random volume over ground (RVoG). For a procedure of reconstruction of vegetation layer parameters, we consider a scenario where the distortions due to dFR are handled as if they are caused by noise. The resulting errors in the vegetation layer parameters are used as a measure of the dFR effect on PolInSAR reconstruction.

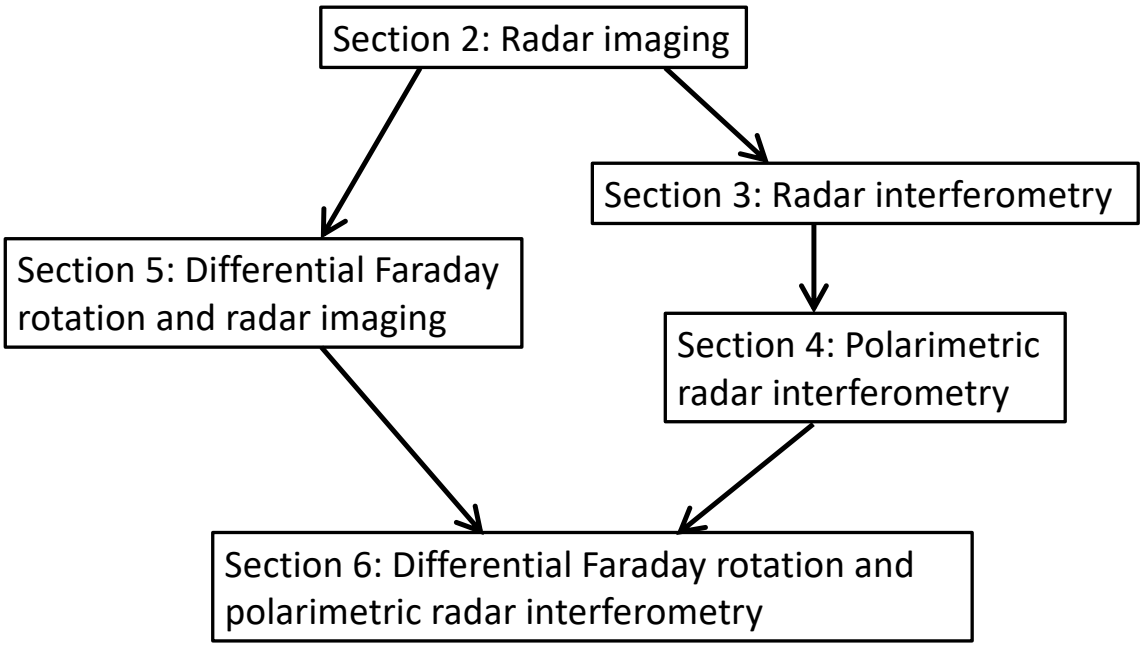

Figure 1: Organization of Sections 2–5 that present background material for Section 6.

In Sections 2–5 we briefly review the necessary background for this study, namely, the radar imaging (SAR), radar interferometry (InSAR), polarimetric radar interferometry (PolInSAR), and differential Faraday rotation (dFR), respectively, see Fig. 1. Section 6.1 introduces a simplified RVoG model that is used in the subsequent imaging and parameter reconstruction scenarios. Section 6.2 presents a scenario where dFR distorts the measurements, whereas Section 6.3 discusses the the effect of noise on the measurements and its compensation in the parameter reconstruction. Ultimately, Section 6.4 presents a combination of the two aforementioned scenarios: the distortions due to dFR are compensated as if they originate from noise. The reconstruction errors obtained in this scenario are summarized and analyzed in Section 7, while discussion in Section 8 reveals certain areas where the approach of this article can be refined. Section 9 provides concluding remarks.

A note about the terminology is in order. The significance of synthetic aperture in SAR

imaging is to provide the along-track resolution. At the same time, the analysis of radar interferometry, as well as polarimetric radar interferometry, usually occurs in the cross-track plane. In this work, we do not consider the effects due to the presence of a synthetic aperture. For this reason, we use the term "radar interferometry" instead of more common abbreviations InSAR and PolInSAR whenever this would not lead to misunderstanding.

2 Radar imaging, reflectivity, and imaging kernel

Following [25, Chapter 2], we specify, for definiteness, the antenna signal as a narrow-band linear chirp (frequency modulated signal) with the carrier frequency ω_0, bandwidth B, duration τ, and rate $\alpha > 0$ related by

$$2\alpha\tau = B \ll \omega_0 \quad \text{and} \quad B\tau \gg 1.$$

Using the notation $\chi_{_\tau}$ for the characteristic function:

$$\chi_{_\tau}(t) = \begin{cases} 1, & t \in [-\tau/2, \tau/2], \\ 0, & \text{otherwise}, \end{cases} \tag{1}$$

we can write the expression for the chirp waveform as follows:

$$P(t) = A(t)e^{-i\omega_0 t}, \quad \text{where} \quad A(t) = \chi_{_\tau}(t)e^{-i\alpha t^2}. \tag{2}$$

For simplicity, we analyze only the case of $\alpha > 0$. One can derive the expression for the instantaneous frequency by differentiating (2) with respect to t inside the support of $A(t)$:

$$\omega(t) = \omega_0 + 2\alpha t = \omega_0 + \frac{B}{\tau}t, \quad |t| \leqslant \frac{\tau}{2}. \tag{3}$$

The antenna is at location $\boldsymbol{x}$, which may be either of the two locations, $\boldsymbol{x}^{(0)}$ or $\boldsymbol{x}^{(1)}$, in Fig. 2, separated from the target area by the distance R. Propagation of a signal is described by means of propagation attenuation and time delay, such that the incident field u^{i} in the target area is described by

$$u^{\mathrm{i}}(t, \boldsymbol{z}) = K(R_{\boldsymbol{z}})P(t - R_{\boldsymbol{z}}/c), \tag{4}$$

where c is the speed of light and

$$R_{\boldsymbol{z}} = |\boldsymbol{z} - \boldsymbol{x}|.$$

We assume a point scatterer at $\boldsymbol{z}$ with the reflectivity ν_0, such that the reflected field is given by

$$u^{\mathrm{s}}(t, \boldsymbol{z}) = \nu_0 u^{\mathrm{i}}(t, \boldsymbol{z}) = \nu_0 K(R_{\boldsymbol{z}})P(t - R_{\boldsymbol{z}}/c). \tag{5}$$

The field received by the antenna is calculated similarly to (4):

$$u^{\mathrm{s}}(t, \boldsymbol{x}) = K(R_{\boldsymbol{z}})u^{\mathrm{s}}(t - R_{\boldsymbol{z}}/c, \boldsymbol{z}) = \nu_0 K(R_{\boldsymbol{z}})^2 P(t - 2R_{\boldsymbol{z}}/c).$$

This expression can be seen as a particular case of the return from a distributed scatterer calculated in the single-scattering approximation [25, 3]:

$$u^{\mathrm{s}}(t,\boldsymbol{x}) = \int \nu(\boldsymbol{z}')K(R_{\boldsymbol{z}'})^2 P(t-2R_{\boldsymbol{z}'}/c)\,d\boldsymbol{z}', \tag{6}$$

with the singular reflectivity function

$$\nu(\boldsymbol{z}') = \nu_0\delta(\boldsymbol{z}'-\boldsymbol{z}), \tag{7}$$

where $\delta(\ldots)$ is the Dirac delta function. While the fields vary on the scale of the wavelength $\lambda = 2\pi c/\omega_0$, the attenuation coefficient varies on a much larger scale of R, e.g., $K(R_{\boldsymbol{z}}) \sim R_{\boldsymbol{z}}^{-1}$. Hence, given that the size of the target is much smaller that a typical travel distance, we can replace $K(R_{\boldsymbol{z}})$ and $K(R_{\boldsymbol{z}'})$ in (4)–(6) with a constant $K(R)$. Furthermore, for the sake of brevity, we will henceforth incorporate the constant $K(R)^2$ into ν_0 and/or $\nu(\boldsymbol{z})$.

Approximate inversion of (6) for $\nu(\boldsymbol{z}')$ is realized by application of a matched filter to the received signal. The matched filter P_{filt} is a complex conjugate of the antenna signal (2); it is parametrized by $\boldsymbol{y}$, which is the spatial argument of the image:

$$P_{\mathrm{filt}}(t;\boldsymbol{y}) = \overline{P(t-t_{\boldsymbol{y}})}, \quad \text{where} \quad t_{\boldsymbol{y}} = \frac{2|\boldsymbol{y}-\boldsymbol{x}|}{c} = \frac{2R_{\boldsymbol{y}}}{c}. \tag{8}$$

Accordingly, the image (i.e., the approximation to $\nu(\cdot)$ of (6)) is expressed as

$$I(\boldsymbol{y}) = \int P_{\mathrm{filt}}(t;\boldsymbol{y})u^{\mathrm{s}}(t,\boldsymbol{x})\,dt = \int \overline{P\Big(t-\frac{2R_{\boldsymbol{y}}}{c}\Big)}u^{\mathrm{s}}(t,\boldsymbol{x})\,dt. \tag{9}$$

We will call $R_{\boldsymbol{y}} = |\boldsymbol{y}-\boldsymbol{x}|$ the focusing parameter of the filter.

Substituting (6) into (9), we obtain the convolution formula

$$I(\boldsymbol{y}) = \int W(\boldsymbol{y},\boldsymbol{z})\nu(\boldsymbol{z})\,d\boldsymbol{z}, \tag{10}$$

where the kernel of the imaging operator (also called the point spread function, or PSF) is given by

$$W(\boldsymbol{y},\boldsymbol{z}) = \int \overline{P\Big(t-\frac{2R_{\boldsymbol{y}}}{c}\Big)}P\Big(t-\frac{2R_{\boldsymbol{z}}}{c}\Big)\,dt = e^{-2ik(R_{\boldsymbol{y}}-R_{\boldsymbol{z}})}V(\boldsymbol{y},\boldsymbol{z}). \tag{11}$$

In (11), $k = \omega_0/c$ and

$$\begin{aligned} V(\boldsymbol{y},\boldsymbol{z}) &= \int \overline{A\Big(t-\frac{2R_{\boldsymbol{y}}}{c}\Big)}A\Big(t-\frac{2R_{\boldsymbol{z}}}{c}\Big)\,dt \\ &\approx \int_{-\tau/2}^{\tau/2} e^{-4i\alpha(R_{\boldsymbol{y}}-R_{\boldsymbol{z}})\tilde{t}/c}\,d\tilde{t} \\ &= \tau\,\mathrm{sinc}\,\Big(\frac{B(R_{\boldsymbol{y}}-R_{\boldsymbol{z}})}{c}\Big), \end{aligned} \tag{12}$$

where $\mathrm{sinc}(\xi) = \sin(\xi)/\xi$. Hence, for signal $P(t)$ given by (2), the kernel depends on the difference of the focusing parameters: $W = W(R_{\boldsymbol{y}} - R_{\boldsymbol{z}})$, so formula (10) can be presented as

$$I(\boldsymbol{y}) = \int W(R_{\boldsymbol{y}} - R_{\boldsymbol{z}})\nu(\boldsymbol{z})\, d\boldsymbol{z}, \tag{13}$$

where according to (11),(12), the PSF $W(l)$ can be expressed as the following function:

$$W(l) = e^{-2ikl}V(l) = \tau e^{-2ikl}\,\mathrm{sinc}\left(\frac{Bl}{c}\right). \tag{14}$$

Hence, for the point scatterer (7), the expression for the image is as follows:

$$I(\boldsymbol{y}) = \nu_0 \cdot \tau e^{-2i\omega_0(R_{\boldsymbol{y}} - R_{\boldsymbol{z}})/c}\,\mathrm{sinc}\left(B\frac{R_{\boldsymbol{y}} - R_{\boldsymbol{z}}}{c}\right). \tag{15}$$

In the two-dimensional coordinate space $\boldsymbol{z}$ considered in this work, the main lobe of the sinc function in (15) specifies a ring of average radius $R_{\boldsymbol{y}}$ and thickness about

$$\Delta_{\mathrm{R}} = \frac{\pi c}{B}.$$

Although the function $|I(\boldsymbol{y})|$ given by (15) has a single maximum at $R_{\boldsymbol{y}} = R_{\boldsymbol{z}}$, locating it with the accuracy much better than Δ_{R} is considered problematic in practical situations where contributions from other scatterers, as well as noise, are present. As the radius of the ring is very large, in the vicinity of the target this ring can be considered as a band with width $\sim \Delta_{\mathrm{R}}$. Obtaining resolution along this band in SAR imaging with kernel (14) is impossible.

In this work, we will be using the term "pixel" to in the context of a pair of locations, $\boldsymbol{y}$ and $\boldsymbol{z}$, satisfying

$$B\frac{|R_{\boldsymbol{y}} - R_{\boldsymbol{z}}|}{c} \lesssim 1. \tag{16}$$

In other words, when points $\boldsymbol{y}$ and $\boldsymbol{z}$ are in one pixel, they can be covered by a single band described above. Similarly, points $\boldsymbol{z}$ and $\boldsymbol{z}'$ are in the same pixels if there is a point $\boldsymbol{y}$ in a pixel with either of them. When condition (16) is not satisfied, we will say that $\boldsymbol{y}$ and $\boldsymbol{z}$ belong to different pixels, etc. Note that this definition is made for convenience of presentation and does not imply any regular or irregular tiling of the space of $\boldsymbol{y}$ (or $\boldsymbol{z}$).

3 Radar interferometry

In radar interferometry [1, 2], especially when combined with polarimetry as in Section 4, stochastic target models are often used to represent extended scatterers. In particular, the reflectivity function $\nu(\boldsymbol{z})$ is considered a circular Gaussian random function [26] with certain correlation properties. The most common example is a delta-correlated scatterer:

$$\langle\overline{\nu(\boldsymbol{z}')}\nu(\boldsymbol{z})\rangle = \sigma^2(\boldsymbol{z})\delta(\boldsymbol{z}' - \boldsymbol{z}), \tag{17}$$

where $\langle\ldots\rangle$ denotes statistical averaging (in practical settings replaced with spatial averaging over a patch of terrain that is assumed homogeneous). Accordingly, the scattered field (6)

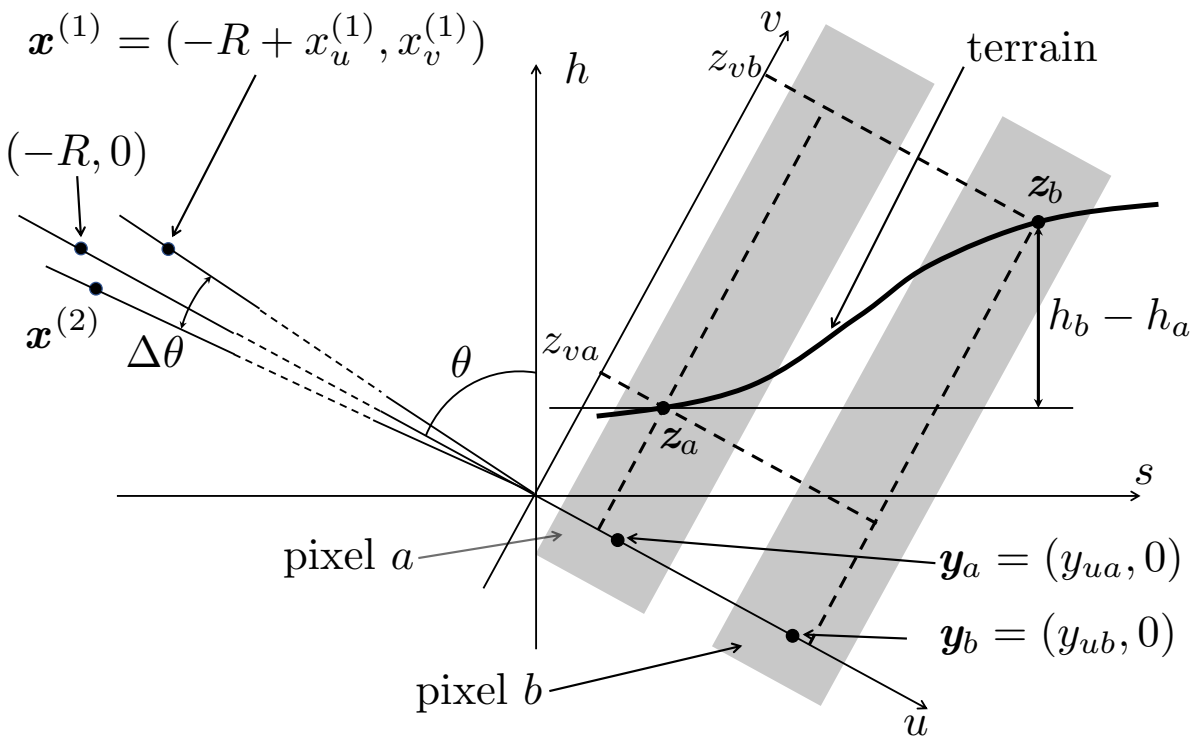

Figure 2: Main geometric parameters of radar interferometry. For definition of pixel see (16).

and radar image (9) are also considered as random functions. Note that the left hand side of (17) is undefined for the reflectivity function of a point scatterer (7) containing the Dirac delta function, so there is no "smooth transition" from model (7) to model (17).

Radar interferometry involves two or more antenna locations, as shown in Fig. 2. A slanted (u, v) coordinate system is used to define the satellite and terrain coordinates, e.g., $\boldsymbol{x}^{(1)} = (-R + x_u^{(1)}, x_v^{(1)})$. The reference satellite position $(-R, 0)$ specifies the reference incidence angle θ, whereas the satellites located at $\boldsymbol{x}^{(1)}$ and $\boldsymbol{x}^{(2)}$ correspond to slightly different individual incidence angles θ_1 and θ_2, respectively, given by

$$\theta_1 \approx \theta - \frac{x_v^{(1)}}{R}, \quad \theta_2 \approx \theta - \frac{x_v^{(2)}}{R}, \quad \Delta\theta = \theta_1 - \theta_2. \tag{18}$$

For a task of reconstruction of the scatterer elevation, we use a complex interferogram defined as follows [6]. First, we introduce an extended notation for the radar image $I(\boldsymbol{y})$ originally defined in (9); this notation specifies the antenna position, carrier frequency, and bandwidth:

$$I(\boldsymbol{y}) \equiv I(\boldsymbol{y}; \boldsymbol{x}, \omega, \tilde{B}),$$

such that we can consider images built using different antenna positions, different central frequencies, and bandwidths different from the full signal bandwidth B. In addition, we introduce an alternative form of the image:

$$\mathcal{I}(\boldsymbol{y}; \boldsymbol{x}, \omega, \tilde{B}) = I(\boldsymbol{y}; \boldsymbol{x}, \omega, \tilde{B}) e^{2i\omega|\boldsymbol{y}-\boldsymbol{x}|/c}. \tag{19}$$

The alternative image definition (19) is needed to reduce sensitivity of the interferogram phase to the focusing parameter $\boldsymbol{y}$,

Then, with the focusing locations restricted to $y_v = 0$ [6], the two images must be co-registered [27], and the interferogram is formed according to

$$Q(\boldsymbol{y}) \equiv Q(\boldsymbol{y}; \boldsymbol{x}^{(1)}, \boldsymbol{x}^{(2)}, \omega_1, \omega_2, \tilde{B}) = \Big\langle \overline{\mathcal{I}(\boldsymbol{y}^{(1)}; \boldsymbol{x}^{(1)}, \omega_1, \tilde{B})} \mathcal{I}(\boldsymbol{y}^{(2)}; \boldsymbol{x}^{(2)}, \omega_2, \tilde{B}) \Big\rangle. \tag{20}$$

In formula (20), $\boldsymbol{y}^{(1)}$ and $\boldsymbol{y}^{(2)}$ are sufficiently close to $\boldsymbol{y}$ owing to the co-registration:

$$|\boldsymbol{y}^{(1)} - \boldsymbol{y}| \ll \Delta_{\mathrm{R}}, \quad |\boldsymbol{y}^{(2)} - \boldsymbol{y}| \ll \Delta_{\mathrm{R}},$$

and parameters ω_1, ω_2, and $\tilde{B}$ are chosen such that for the two systems, the ranges of wavenumbers (i.e., spatial frequencies) projected on the horizontal plane coincide. For a pair of satellites using the same waveform (2), this condition is met by extracting subbands of the original frequency band $\big(\omega_0 - \frac{B}{2}, \omega_0 + \frac{B}{2}\big)$. Using the interferometric angle $\Delta\theta = \theta_1 - \theta_2$, $|\Delta\theta| \ll 1$, see (18), the bandwidth $\tilde{B}$ and the central wavenumbers

$$k_1 = \omega_1/c \quad \text{and} \quad k_2 = \omega_2/c \tag{21a}$$

are determined as follows:

$$k_1 = k - \frac{\Delta k}{2}, \quad k_2 = k + \frac{\Delta k}{2}, \quad \tilde{B} = B - |\Delta k| c, \quad \text{where} \quad \Delta k = k \frac{\Delta\theta}{\tan\theta}. \tag{21b}$$

For the frequencies ω_1 and ω_2 defined via (21a), formula (21b) provides the required relation for the horizontal components of the central wavenumbers:

$$k_1 \sin\theta_1 \approx k_2 \sin\theta_2. \tag{22}$$

Hence, the ranges of the horizontal spatial frequencies coincide because the same bandwidth $\tilde{B}$ is used for both satellites. The condition $\tilde{B} > 0$ together with $B \ll \omega_0$ limits the maximal interferometric angle to

$$|\Delta\theta| < \tan\theta \frac{B}{\omega_0} \ll 1. \tag{23}$$

The subband selection as in (21) is sometimes called wavenumber adjustment procedure or range spectral filtering [6].

For the imaging kernel (11), scatterer (17), and interferometric parameters satisfying (21), the interferogram (20) is expressed as follows [6]:

$$Q(\boldsymbol{y}) = e^{i\Phi_Q} \int e^{-i\kappa h(\boldsymbol{z})} |\tilde{V}(\boldsymbol{y}, \boldsymbol{z})|^2 \sigma^2(\boldsymbol{z})\, d\boldsymbol{z}, \tag{24}$$

where

$$\kappa = 2k \frac{\Delta\theta}{\sin\theta} \tag{25}$$

is called the interferometric wavenumber, $h(\boldsymbol{z})$ is the elevation of point $\boldsymbol{z}$ above the reference horizontal plane $h = 0$ (see Fig. 2), function $\tilde{V}(l)$ is a counterpart to $V(l)$ of (12),(14):

$$\tilde{V}(l) = \tilde{\tau}\, \mathrm{sinc}\Big(\frac{\tilde{B} l}{c}\Big), \quad \text{with} \quad \tilde{\tau} = \tau \frac{\tilde{B}}{B}, \quad \tilde{B} \text{ given by (21b)}, \tag{26}$$

and Φ_Q is a common interferometric phase determined by the exact location of the satellites with respect to the reference plane:

$$\Phi_Q = 2k\Big(-\big(x_u^{(2)} - x_u^{(1)}\big) + \frac{\big(x_v^{(2)}\big)^2 - \big(x_v^{(1)}\big)^2}{2R}\Big) + \Delta k(2R - x_u^{(1)} - x_u^{(2)}). \tag{27}$$

Note that the wavenumber adjustment procedure (21),(22) has eliminated dependence of the interferometric phase in the integrand of (24) on the horizontal coordinate, thus increasing coherence of an interferogram in the case of extended scatterers; for more detail, see, e.g., [6, 28, 29].

Due to uncertainties in several parameters entering the right hand side of (27), evaluating Φ_Q accurate to a fraction of π from the satellite coordinates is deemed impossible. However, retrieval of the relative scatterer elevation is still possible in the following settings. Consider two distinct pixels, a and b, see (16) and Fig. 2, and suppose the scatterer elevation is (nearly) constant in each of them. This means that the scatterer reflectivity $\sigma^2(\boldsymbol{z})$ in these pixels can be approximated by

$$\sigma^2(\boldsymbol{z}) = \sigma_a^2\delta(h(\boldsymbol{z}) - h_a) \quad \text{and} \quad \sigma^2(\boldsymbol{z}) = \sigma_b^2\delta(h(\boldsymbol{z}) - h_b), \tag{28}$$

respectively. Then, from (24), we obtain

$$\frac{Q(\boldsymbol{y}_b)}{Q(\boldsymbol{y}_a)} = \frac{\sigma_b^2}{\sigma_a^2} e^{-i\kappa(h_b - h_a)},$$

such that the height difference between these pixels can be retrieved from the interferogram using

$$h_b - h_a = -\frac{\angle Q(\boldsymbol{y}_b) - \angle Q(\boldsymbol{y}_a)}{\kappa}.$$

As the complex phase is bounded, e.g., $0 \leqslant \big|\angle\big(Q(\boldsymbol{y}_b)/Q(\boldsymbol{y}_a)\big)\big| < \pi$, the reconstructed height difference cannot exceed a certain threshold:

$$|h_b - h_a| < \pi\frac{\sin\theta}{2k\Delta\theta} = \frac{\lambda\sin\theta}{4\Delta\theta}. \tag{29}$$

The value on the right hand side of (29) is half of what is called the ambiguity height (i.e., the change in elevation resulting the change of the interferometric phase by 2π, see, e.g., [30, 31]). In practice, elevations larger than the threshold (29) are reconstructed using the technique of phase unwrapping, see, e.g., [32, 33, 34]. For brevity, we will assume below that condition (29) and its equivalents are always met.

4 Polarimetric radar interferometry

Polarimetric radar interferometry (often abbreviated as PolInSAR) seeks to reconstruct the behavior of $\sigma^2(\boldsymbol{z})$ on the vertical coordinate h from the measurements of interferometric coherence $Q(\boldsymbol{y})$ of (20) at different polarizations. In particular, when

$$\sigma^2(\boldsymbol{z}) \equiv \sigma^2(h(\boldsymbol{z})) \tag{30}$$

(note the difference with (28)), it is shown (see, e.g., [2, 6]) that expression (24) can be factored as follows:

$$Q = e^{i\Phi_Q} V_Q \int e^{-i\kappa h} \sigma^2(h)\, dh, \tag{31}$$

where

$$V_Q = \int |\tilde{V}(s \sin\theta)|^2\, ds, \tag{32}$$

and $\tilde{V}$ is defined in (26). The dependence of Q on $\boldsymbol{y}$ in (31) can be restored by assuming that the parameters defining the function $\sigma^2(h)$ in (30) are constant over a spatial patch mentioned after (17) but may still vary over the horizontal coordinates on distances much larger than the size of this patch (see, e.g., (28)). Such an assumption is meaningful because the integrand in (32) decays quickly on scales much larger than the pixel size $\pi c/\tilde{B}$, so $Q(\boldsymbol{y})$ is mainly affected by the scatterers within the corresponding pixel, see Fig. 3.

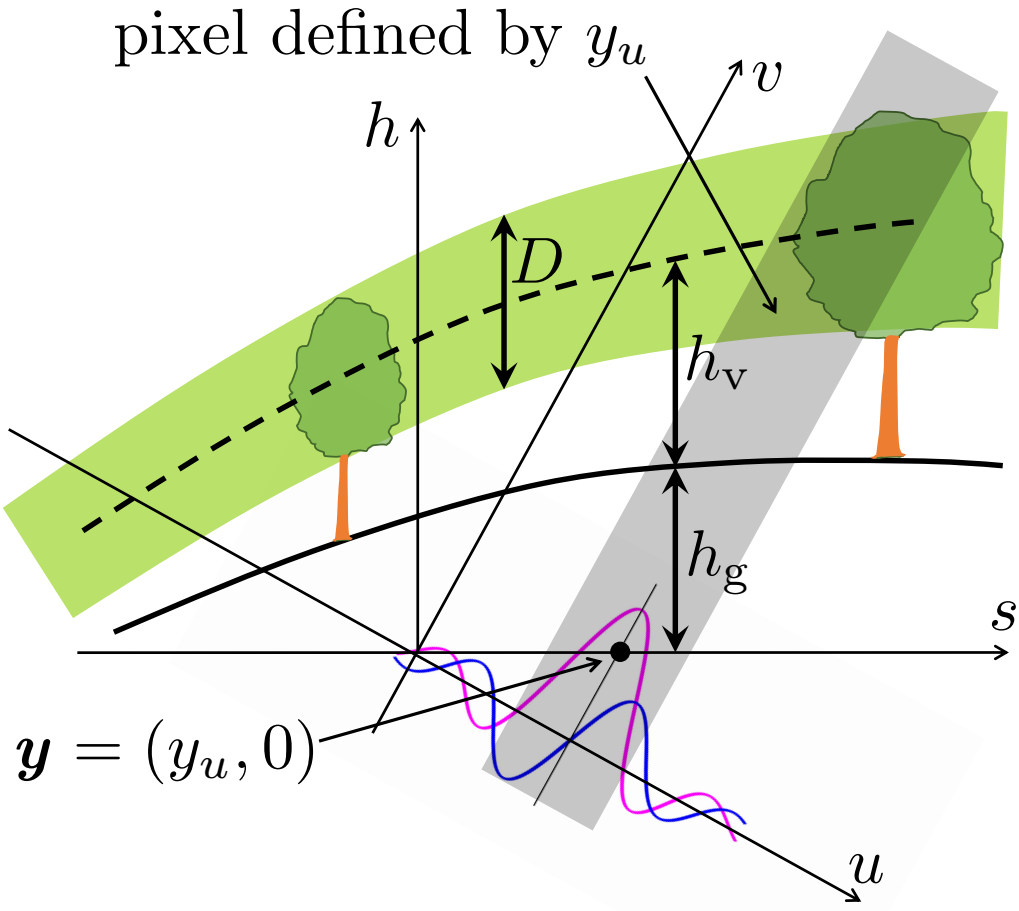

Figure 3: Parameters of ground topography and vegetation layer in RVoG model as given by (35). Note that the real terrain slopes are usually much smaller than on this illustration, so these parameters can be considered constant in each pixel. The purple and blue curves illustrate $F_0(\xi;\eta)$ and $\eta^{-1}F_1(\xi;\eta)$, respectively, see (64), for small η and $\xi = \tilde{B}(y_u - z_u)/c$.

Of course, function $\sigma^2(h)$ cannot be reconstructed from (31) with a single value of Q as data, even more so given the unknown value of Φ_Q. The PolInSAR approach is to obtain

measurements of Q on multiple polarizations and use a parametrized form of $\sigma^2(h)$ with some specific assumptions about its polarimetric behavior. A typical model will represent the reflectivity as a sum of a few components with different localization in height and different dependence of the reflectivity on the polarization[1] (traditionally denoted by symbol $\mathbf{w}$). The most popular model of this kind, called random volume over ground (RVoG), includes two statistically independent terms representing ground and volume (i.e., foliage):

$$\nu(\boldsymbol{z},\mathbf{w}) = \nu_{\mathrm{Gr}}(\boldsymbol{z},\mathbf{w}) + \nu_{\mathrm{Vol}}(\boldsymbol{z},\mathbf{w}), \quad \langle\overline{\nu_{\mathrm{Gr}}(\boldsymbol{z},\mathbf{w})}\nu_{\mathrm{Vol}}(\boldsymbol{z},\mathbf{w})\rangle = 0. \tag{33}$$

Additionally, it is assumed that ν_{Gr} and ν_{Vol} in (33) separately satisfy (17) and (30):

$$\begin{aligned}\langle\overline{\nu_{\mathrm{Gr}}(\boldsymbol{z}',\mathbf{w})}\nu_{\mathrm{Gr}}(\boldsymbol{z},\mathbf{w})\rangle &= \sigma^2_{\mathrm{Gr}}(h,\mathbf{w})\delta\big(h(\boldsymbol{z}') - h(\boldsymbol{z})\big),\\ \langle\overline{\nu_{\mathrm{Vol}}(\boldsymbol{z}',\mathbf{w})}\nu_{\mathrm{Vol}}(\boldsymbol{z},\mathbf{w})\rangle &= \sigma^2_{\mathrm{Vol}}(h,\mathbf{w})\delta\big(h(\boldsymbol{z}') - h(\boldsymbol{z})\big),\end{aligned}$$

leading to the following relation between the reflectivity intensities:

$$\sigma^2(h,\mathbf{w}) = \sigma^2_{\mathrm{Gr}}(h,\mathbf{w}) + \sigma^2_{\mathrm{Vol}}(h,\mathbf{w}). \tag{34}$$

For σ^2_{Gr} and σ^2_{Vol} in (34), we will use the following parametrization of their dependence on h:

$$\begin{aligned}\sigma^2_{\mathrm{Gr}}(h,\mathbf{w}) &= \sigma^2_{\mathrm{g}}(\mathbf{w})\delta(h - h_{\mathrm{g}}),\\ \sigma^2_{\mathrm{Vol}}(h,\mathbf{w}) &= \sigma^2_{\mathrm{v}}(\mathbf{w})\frac{1}{D}\chi_D(h - h_{\mathrm{g}} - h_{\mathrm{v}}).\end{aligned} \tag{35}$$

In formula (35), h_{g} describes the ground topography, h_{v} and D denote the average elevation and thickness of a foliage layer, see Fig. 3, and the indicator function χ is defined in (1). A possible formulation of PolInSAR inversion is to retrieve the constants h_{v} and D characterizing the vegetation (e.g., the forest height will be given by $h_{\mathrm{v}} + D/2$) and h_{g} providing the local ground elevation.

As mentioned following (32), the values of h_{g}, h_{v}, and D in (35) can be considered constant over a patch of pixels used to calculate $Q(\boldsymbol{y})$; the same is assumed about $\sigma^2_{\mathrm{g}}(\mathbf{w})$ and $\sigma^2_{\mathrm{v}}(\mathbf{w})$ for fixed $\mathbf{w}$. For this reason, we will drop the argument $\boldsymbol{y}$ whenever possible in the remainder of this section to improve readability while keeping the dependence on $\mathbf{w}$. If we consider image components $\mathcal{I}_{\mathrm{Gr}}(\mathbf{w})$ and $\mathcal{I}_{\mathrm{Vol}}(\mathbf{w})$ due to individual scatterers at certain polarizations, such that

$$\mathcal{I}(\mathbf{w}) = \mathcal{I}_{\mathrm{Gr}}(\mathbf{w}) + \mathcal{I}_{\mathrm{Vol}}(\mathbf{w}), \tag{36}$$

then, due to (33),

$$Q(\mathbf{w}) = Q_{\mathrm{Gr}}(\mathbf{w}) + Q_{\mathrm{Vol}}(\mathbf{w}),$$

where, similarly to (20),

$$\begin{aligned}Q_{\mathrm{Gr}}(\mathbf{w}) &= \Big\langle\overline{\mathcal{I}_{\mathrm{Gr}}(\mathbf{w};\boldsymbol{x}^{(1)},\ldots)}\mathcal{I}_{\mathrm{Gr}}(\mathbf{w};\boldsymbol{x}^{(2)},\ldots)\Big\rangle,\\ Q_{\mathrm{Vol}}(\mathbf{w}) &= \Big\langle\overline{\mathcal{I}_{\mathrm{Vol}}(\mathbf{w};\boldsymbol{x}^{(1)},\ldots)}\mathcal{I}_{\mathrm{Vol}}(\mathbf{w};\boldsymbol{x}^{(2)},\ldots)\Big\rangle.\end{aligned}$$

[1] In this section, it is sufficient to treat the word "polarization" as some hidden parameter of reflectivity and imaging. A more physics-aware treatment of polarization is given in Section 5.

In order to calculate interferometric coherence, we define the image intensities

$$T^{(1)}(\mathbf{w}) = \left\langle \left|\mathcal{I}(\mathbf{w}; \boldsymbol{x}^{(1)}, k_1, \tilde{B})\right|^2 \right\rangle, \quad T^{(2)}(\mathbf{w}) = \left\langle \left|\mathcal{I}(\mathbf{w}; \boldsymbol{x}^{(2)}, k_2, \tilde{B})\right|^2 \right\rangle, \tag{37}$$

cf. (20), and assume that

$$T^{(1)}(\mathbf{w}) \approx T^{(2)}(\mathbf{w}) = T(\mathbf{w}) \tag{38}$$

because the imaging conditions for the two antennas are essentially equivalent, see (23). The total coherence and the coherences of individual image components are defines as follows:

$$\gamma(\mathbf{w}) = \frac{Q(\mathbf{w})}{T(\mathbf{w})}, \quad \gamma_{\mathrm{Gr}}(\mathbf{w}) = \frac{Q_{\mathrm{Gr}}(\mathbf{w})}{T_{\mathrm{Gr}}(\mathbf{w})}, \quad \gamma_{\mathrm{Vol}}(\mathbf{w}) = \frac{Q_{\mathrm{Vol}}(\mathbf{w})}{T_{\mathrm{Vol}}(\mathbf{w})}. \tag{39}$$

A derivation similar to that used for (24) and (31) leads to

$$T(\boldsymbol{y}, \mathbf{w}) = \int |\tilde{V}(\boldsymbol{y}, \boldsymbol{z})|^2 \sigma^2(\boldsymbol{z}, \mathbf{w})\, d\boldsymbol{z} = V_Q \int \sigma^2(h)\, dh, \tag{40}$$

where, similarly to $Q(\mathbf{w})$, we will henceforth replace $T(\boldsymbol{y}, \mathbf{w})$ with $T(\mathbf{w})$. Substituting the parametrizations (35) into (31) and (40) and making a change of variables $h' = h - h_{\mathrm{g}}$, we can explicitly calculate the individual coherences in (39):

$$\begin{aligned} &\gamma_{\mathrm{Gr}} = e^{i(\Phi_Q - \kappa h_{\mathrm{g}})}\gamma_{\mathrm{g}}, \quad \text{where} \quad \gamma_{\mathrm{g}} = \int e^{-i\kappa h'} \delta(h')\, dh' = 1; \\ &\gamma_{\mathrm{Vol}} = e^{i(\Phi_Q - \kappa h_{\mathrm{g}})}\gamma_{\mathrm{v}}, \quad \text{where} \quad \gamma_{\mathrm{v}} = \frac{1}{D}\int_{h_{\mathrm{v}} - D/2}^{h_{\mathrm{v}} + D/2} e^{-i\kappa h'}\, dh' = e^{-i\kappa h_{\mathrm{v}}}\, \mathrm{sinc}(\kappa D/2); \end{aligned} \tag{41}$$

and $\kappa = 2k\Delta\theta/\sin\theta$ is defined in (25). In turn, using (33)–(35), we can obtain the following relation:

$$\gamma(\mathbf{w}) = \frac{\sigma_{\mathrm{g}}^2(\mathbf{w})}{\sigma_{\mathrm{g}}^2(\mathbf{w}) + \sigma_{\mathrm{v}}^2(\mathbf{w})}\gamma_{\mathrm{Gr}} + \frac{\sigma_{\mathrm{v}}^2(\mathbf{w})}{\sigma_{\mathrm{g}}^2(\mathbf{w}) + \sigma_{\mathrm{v}}^2(\mathbf{w})}\gamma_{\mathrm{Vol}} \tag{42}$$

(see, e.g., [33] and Appendix A). Using (41), we can rewrite relation (42) in the form that is popular in PolInSAR literature [9]:

$$\gamma(\mathbf{w}) = e^{i\Psi_Q}\frac{\gamma_{\mathrm{v}} + m(\mathbf{w})}{1 + m(\mathbf{w})} = e^{i\Psi_Q}\left(\gamma_{\mathrm{v}} + \frac{m(\mathbf{w})}{1 + m(\mathbf{w})}(1 - \gamma_{\mathrm{v}})\right), \tag{43}$$

where

$$\Psi_Q = \Phi_Q - \kappa h_{\mathrm{g}}, \quad m(\mathbf{w}) = \frac{\sigma_{\mathrm{g}}^2(\mathbf{w})}{\sigma_{\mathrm{v}}^2(\mathbf{w})}. \tag{44}$$

Formula (43) can be visualized by a straight line on a complex plane, as illustrated in Fig. 4: each point on an interval between $e^{i\Psi_Q}$ and $e^{i\Psi_Q}\gamma_{\mathrm{v}}$ corresponds to a certain value of $m(\mathbf{w})$, $0 < m(\mathbf{w}) < \infty$.

In PolInSAR inversion procedures, the values of $e^{i\Psi_Q}$ and γ_{v} are reconstructed from the set of relations (43) for different $\mathbf{w}$, while $m(\mathbf{w})$ is considered unknown. In turn, the ground topography, up to a constant reference elevation, can be retrieved from Ψ_Q using (44), while

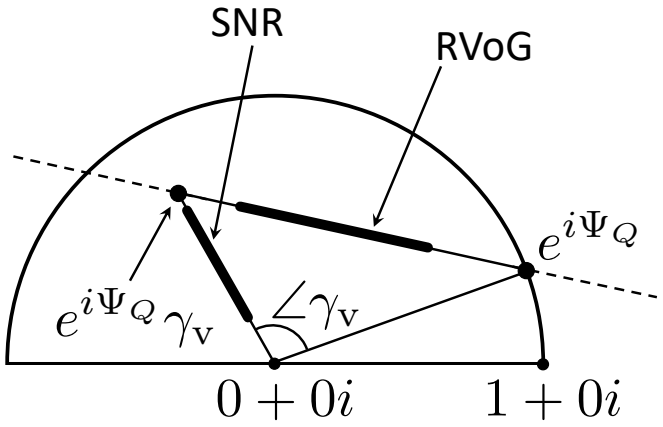

Figure 4: Loci of polarimetric coherence $\gamma(\mathbf{w})$ on a complex plane. The straight line passing through $e^{i\Psi_Q}$ and $e^{i\Psi_Q}\gamma_{\mathrm{v}}$ is given by formula (43), while the interval marked "RVoG" corresponds to $0 < m_{\min} \leqslant m(\mathbf{w}) < \infty$. The interval marked "SNR" corresponds to formula (48) for $0 < \mathrm{SNR}_{\min} \leqslant \mathrm{SNR}(\mathbf{w}) < \infty$.

the average height and thickness of the vegetation layer can be found from $\angle\gamma_{\mathrm{v}}$ and $|\gamma_{\mathrm{v}}|$, respectively, see (41).

Given that the physical differences between the ground and foliage scatterers lead to different behaviors of σ^2_{g} and σ^2_{v} as functions of $\mathbf{w}$, it should be possible to obtain two or more different values of $m(\mathbf{w})$, see (44), resulting in two or more different values of $\gamma(\mathbf{w})$ via (43). Most reconstruction procedures make use of the straight line representation of (43), see Fig. 4. Namely, a straight line fit in the complex plane is built for these values of $\gamma(\mathbf{w})$, and one of two intersections of this line with a unit circle $|\gamma| = 1$ is associated with $e^{i\Psi_Q}$ (this corresponds to $m \to \infty$ in (43), although there may be no $\mathbf{w}$ yielding this data point). Further steps of inversion [28, 35] may assume various physical considerations about $\sigma^2_{\mathrm{g}}(\mathbf{w})$ and $\sigma^2_{\mathrm{v}}(\mathbf{w})$ that are beyond the scope of this work.

The model (34)–(36) permits many extensions that make it more realistic. A very common one is to take into account the damping of the signal due to foliage; in particular, this leads to an exponential rather than constant profile in the model for σ^2_{Vol} in (35), see, e.g., [28]. We will not consider this effect here, but instead take into account noise that may come not only from the receiver, but also from temporal decorrelation, misregistration, etc. [10] To do so, we modify (36) as follows

$$\begin{aligned} \mathcal{I}(\mathbf{w}; \boldsymbol{x}^{(1)}) &= \mathcal{I}_{\mathrm{Gr}}(\mathbf{w}; \boldsymbol{x}^{(1)}) + \mathcal{I}_{\mathrm{Vol}}(\mathbf{w}; \boldsymbol{x}^{(1)}) + N^{(1)}, \\ \mathcal{I}(\mathbf{w}; \boldsymbol{x}^{(2)}) &= \mathcal{I}_{\mathrm{Gr}}(\mathbf{w}; \boldsymbol{x}^{(2)}) + \mathcal{I}_{\mathrm{Vol}}(\mathbf{w}; \boldsymbol{x}^{(2)}) + N^{(2)}, \end{aligned} \tag{45}$$

where the noise terms $N^{(1)}$ and $N^{(2)}$ are circular Gaussian, similarly to the rest of terms in (45), and satisfy

$$\left\langle \overline{N^{(1)}} N^{(2)} \right\rangle = 0, \quad \left\langle |N^{(1)}|^2 \right\rangle = \left\langle |N^{(2)}|^2 \right\rangle = \mathbf{N}^2,$$

where $\mathbf{N}^2$ is noise intensity. As a result, relations (42) and (43) are modified as follows:

$$\begin{aligned}\gamma(\mathbf{w}) &= \frac{V_Q\big(\sigma_{\mathrm{g}}^2(\mathbf{w})\gamma_{\mathrm{Gr}} + \sigma_{\mathrm{v}}^2(\mathbf{w})\gamma_{\mathrm{Vol}}\big)}{V_Q\big(\sigma_{\mathrm{g}}^2(\mathbf{w}) + \sigma_{\mathrm{v}}^2(\mathbf{w})\big) + \mathbf{N}^2} \\ &= e^{i\Psi_Q}\frac{\gamma_{\mathrm{v}} + m(\mathbf{w})}{1 + m(\mathbf{w})} \cdot \frac{\mathrm{SNR}(\mathbf{w})}{1 + \mathrm{SNR}(\mathbf{w})},\end{aligned} \tag{46}$$

where the signal-to-noise ratio is defined by

$$\mathrm{SNR}(\mathbf{w}) = \frac{V_Q\big(\sigma_{\mathrm{g}}^2(\mathbf{w}) + \sigma_{\mathrm{v}}^2(\mathbf{w})\big)}{\mathbf{N}^2}. \tag{47}$$

Consider the case of $m(\mathbf{w}) = 0$: it may represent a cross-polarized scattering channel, either HV or VH, where the ground contribution is low (see, e.g., [36, 37, 28]). A helpful visualization of (46) for this case,

$$\gamma(\mathbf{w}) = e^{i\Psi_Q}\gamma_{\mathrm{v}} \cdot \frac{\mathrm{SNR}(\mathbf{w})}{1 + \mathrm{SNR}(\mathbf{w})}, \tag{48}$$

can be made by observing that the fraction on the right hand side of (48) is real, hence, on the complex plane, $\gamma(\mathbf{w})$ lies on a segment of straight line connecting the origin with $e^{i\Psi_Q}\gamma_{\mathrm{v}}$, as shown in Fig. 4.

The particular cases represented by formulae (43) and (48) will be revisited in Section 6 in the context of polarimetric interferometry in the presence of differential Faraday rotation.

5 Radar imaging in the presence of dFR

The presentation of radar imaging in Section 2 and radar interferometry in Section 3 has been given as if the electromagnetic field were scalar. In Section 4, the concept of polarization has been represented by a variable $\mathbf{w}$ that has not been associated with any physical characteristics of the field. In fact, the electromagnetic field is vector-valued, and the polarization specifies the configuration of electric and magnetic field vectors at the pulse transmit and receive events, as well as for the interaction between the field and the target. For the context of this article, this topic is covered in detail in [11], while a broader scope can be obtained from [38, 28, 39] or classical sources such as [40, 41, 42]. Here we provide a brief summary of facts necessary to introduce the following topics:

- linear polarizations and scattering matrix,
- Faraday rotation (FR), and
- differential Faraday rotation (dFR) and its effect of radar imaging.

Radar imaging typically uses linear polarizations, especially in the geophysical context. Depending on the orientation of the electric field in the incident wave, the polarization is called either horizontal (H) or vertical (V). For any of these two polarizations, the reflected

wave can be represented as a sum of horizontally and vertically polarized waves. This gives rise to a 2×2 scattering (or reflectivity) matrix S relating the incident and reflected fields:

$$\begin{pmatrix} E^{\rm s}_{\rm H} \\ E^{\rm s}_{\rm V} \end{pmatrix}(t, \boldsymbol{z}) = \mathbf{S}(\boldsymbol{z}) \cdot \begin{pmatrix} E^{\rm i}_{\rm H} \\ E^{\rm i}_{\rm V} \end{pmatrix}(t, \boldsymbol{z}), \quad \text{where} \quad \mathbf{S}(\boldsymbol{z}) = \begin{pmatrix} \nu_{\rm HH}(\boldsymbol{z}) & \nu_{\rm HV}(\boldsymbol{z}) \\ \nu_{\rm VH}(\boldsymbol{z}) & \nu_{\rm VV}(\boldsymbol{z}) \end{pmatrix}. \tag{49}$$

This relation is a polarimetric counterpart of the first equality in formula (5), see Section 2.

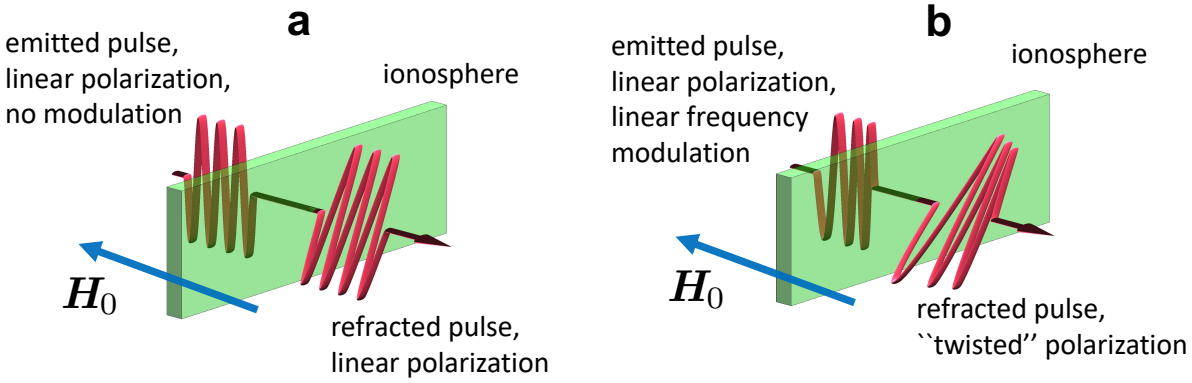

Figure 5: (a) Faraday rotation for a signal without modulation. (b) Differential Faraday rotation for a linear frequency modulated (LFM) signal. The modulation factors and rotation angles are not to scale.

Turning now to propagation of radar pulses, we will have to extend formula (4) to account for the Faraday rotation (FR). Faraday rotation is due to gyrotropy of the ionospheric plasma in the magnetic field of the Earth, and its effect on a monochromatic wave with frequency ω can be described by means of a rotation matrix, see Fig. 5a:

$$\mathbf{R}(\varphi_{\rm F}) = \begin{pmatrix} \cos\varphi_{\rm F} & \sin\varphi_{\rm F} \\ -\sin\varphi_{\rm F} & \cos\varphi_{\rm F} \end{pmatrix}. \tag{50}$$

The rotation angle in formula (50) is given by (see, e.g., [43, 42])

$$\varphi_{\rm F} \equiv \varphi_{\rm F}(\omega) = -\frac{R}{2c}\frac{\omega_{\rm pe}^2 \Omega_{\rm e} \cos\beta}{\omega^2}, \quad \text{where} \quad \omega_{\rm pe}^2 = \frac{4\pi N_{\rm e} e^2}{m_{\rm e}}, \quad \Omega_{\rm e} = -\frac{e|\boldsymbol{H}_0|}{m_{\rm e} c}. \tag{51}$$

In (51), $\omega_{\rm pe}$ and $\Omega_{\rm e}$ are the electron plasma frequency and gyrofrequency, respectively, $m_{\rm e}$ and $-e$ are the mass and charge of the electron, $N_{\rm e}$ denotes the electron number density in the ionosphere, $\boldsymbol{H}_0$ is the magnetic field of the Earth, β is the angle between the wave propagation direction and $\boldsymbol{H}_0$, and we use R instead of $R_{\boldsymbol{z}}$ to simplify the presentation. The resulting propagation formula is

$$\begin{pmatrix} E^{\rm i}_{\rm H} \\ E^{\rm i}_{\rm V} \end{pmatrix}(t, \boldsymbol{z}) = K(R) e^{i\omega R_z / v_{\rm ph}} \mathbf{R}(\varphi_{\rm F}) \cdot \begin{pmatrix} E^{\rm i}_{\rm H} \\ E^{\rm i}_{\rm V} \end{pmatrix}(t, \boldsymbol{x}),$$

where $v_{\rm ph} \approx c$ is the phase speed of electromagnetic waves in the ionosphere.

In order to obtain a polarimetric counterpart of the scalar imaging formula (13), we will take into account the following effects.

1. Dispersive propagation of the radar pulse in plasma leading to the difference between the phase and group speed and the speed of light:

$$v_{\rm ph} = \sqrt{\omega_{\rm pe}^2 + k^2c^2}/k, \quad v_{\rm gr} = kc^2/\sqrt{\omega_{\rm pe}^2 + k^2c^2}$$

(note that for typical radar frequencies, $\omega_{\rm pe}^2 \ll k^2c^2$).

2. Two-way propagation of the electromagnetic pulses, with the accumulation of the rotation angle.

3. Dependence of $\varphi_{\rm F}$ in (50) upon the instantaneous frequency (3) via (51); for a linear frequency modulated signal (2), a linearly polarized emitted signal becomes "twisted" after passing through a dispersive medium, see [11] and Fig. 5b.

The polarimetric image channels are formed by processing the received signal using the matched filter $P'_{\rm filt}(t, \boldsymbol{y})$, which is obtained by modifying the standard filter $P_{\rm filt}$ of (8) according to items 1 and 2 above. As shown in [44, 11], this includes modification of the chirp rate and duration:

$$\alpha' = \alpha + \delta\alpha, \quad \tau' = \tau - \delta\tau, \quad \text{where} \quad \delta\tau = \frac{B}{\omega_0}\frac{R_z}{c}\frac{\omega_{\rm pe}^2}{\omega_0^2}, \quad \delta\alpha = \alpha\frac{\delta\tau}{\tau}, \tag{52}$$

as well as the retarded times, such that

$$P'_{\rm filt}(t, \boldsymbol{y}) = A'(t, \boldsymbol{y})e^{-i\omega_0(t-2R_{\boldsymbol{y}}/v_{\rm ph})},$$

where

$$A'(t, \boldsymbol{y}) = \chi'_{\tau-2\delta\tau}(t - 2R_{\boldsymbol{y}}/v_{\rm gr})e^{-i(\alpha+2\delta\alpha)(t-2R_{\boldsymbol{y}}/v_{\rm gr})^2}. \tag{53}$$

The resulting image channels are considered as entries of a 2×2 matrix $\mathbf{Y}$ organized similarly to (49):

$$Y_{mn}(\boldsymbol{y}) = \int e^{i\omega_0(t-2R_{\boldsymbol{y}}/v_{\rm ph})}\overline{A'(t, \boldsymbol{y})}u^{\rm s}_{mn}(t)\,dt, \quad m, n \in \{\rm H, V\}, \tag{54}$$

where $u^{\rm s}_{mn}(t) = E^{\rm s}_m(t, \boldsymbol{x})$ given the polarization of the emitted field is n. We call matrix $\mathbf{Y}$ an intermediate image.

At the next stage, the average rotation angle is defined as

$$\varphi^*_{\rm F} = \varphi_{\rm F}(\omega_0), \tag{55}$$

see (51), and rotation matrices $\mathbf{R}(-\varphi^*_{\rm F})$ are applied to the intermediate image yielding four entries of a similarly organized 2×2 polarimetric image matrix $\mathbf{I}$:

$$\mathbf{I}(\boldsymbol{y}) = \mathbf{R}(-\varphi^*_{\rm F}) \cdot \mathbf{Y}(\boldsymbol{y}) \cdot \mathbf{R}(-\varphi^*_{\rm F}). \tag{56}$$

Usage of an average rotation angle in (54),(56) creates a mismatch between the actual rotation angle and $\varphi^*_{\rm F}$:

$$\Delta\varphi_{\rm F} \equiv \Delta\varphi_{\rm F}(t, \boldsymbol{z}) = \varphi_{\rm F}\big(\omega(t - 2R_{\boldsymbol{z}}/c)\big) - \varphi^*_{\rm F}, \tag{57}$$

see item 3 on page 16. Note that in [11], we put forward and analyze the polarimetric matched filter (PMF) that compensates the dependence of the Faraday rotation on instantaneous frequency. Unlike (54), this approach requires matrix-based operations on the received signal channels $u^{\mathrm{s}}_{mn}(t)$, with the matrix also depending on time. To save space, the interferometry that uses PMF-based signal processing is not considered here.

To describe the polarimetric imaging operator, we flatten the reflectivity and image matrices:

$$\boldsymbol{I} = (I_{\mathrm{HH}}, I_{\mathrm{HV}}, I_{\mathrm{VH}}, I_{\mathrm{VV}})^{\mathrm{T}}, \quad \boldsymbol{\nu} = (\nu_{\mathrm{HH}}, \nu_{\mathrm{HV}}, \nu_{\mathrm{VH}}, \nu_{\mathrm{VV}})^{\mathrm{T}},$$

and present the relation between them as follows:

$$\boldsymbol{I}(\boldsymbol{y}) = \int \mathbf{W}(\boldsymbol{y}, \boldsymbol{z}) \cdot \boldsymbol{\nu}(\boldsymbol{z})\, d\boldsymbol{z}, \tag{58}$$

where a 4×4 matrix $\mathbf{W}$ can be approximated using another 4×4 matrix $\mathbf{V}$:

$$\mathbf{W}(\boldsymbol{y}, \boldsymbol{z}) = e^{-2ik(R_{\boldsymbol{y}} - R_{\boldsymbol{z}})} \int \overline{A\Big(t - \frac{2R_{\boldsymbol{y}}}{c}\Big)} A\Big(t - \frac{2R_{\boldsymbol{z}}}{c}\Big) \mathbf{V}(\Delta\varphi_{\mathrm{F}})\, dt, \tag{59}$$

with $\Delta\varphi_{\mathrm{F}}(t, \boldsymbol{z})$ given by (57) and

$$\mathbf{V}(\phi) = \begin{pmatrix} \cos^2\phi & -\cos\phi\sin\phi & \cos\phi\sin\phi & -\sin^2\phi \\ \cos\phi\sin\phi & \cos^2\phi & \sin^2\phi & \cos\phi\sin\phi \\ -\cos\phi\sin\phi & \sin^2\phi & \cos^2\phi & -\cos\phi\sin\phi \\ -\sin^2\phi & -\cos\phi\sin\phi & \cos\phi\sin\phi & \cos^2\phi \end{pmatrix}. \tag{60}$$

Note that it is possible to express the entire dFR effect via the matrix $\mathbf{V}$ in (59); in particular, instead of $A'(\ldots)$ defined in (52)–(53), equation (59) makes use of the original pulse envelope $A(t)$ given by (2) [11].

Linearization of $\varphi_{\mathrm{F}}(\omega)$ about ω_0 in (57) yields

$$\Delta\varphi_{\mathrm{F}} \approx \eta \frac{1}{\tau}\Big(t - \frac{2R_{\boldsymbol{z}}}{c}\Big), \quad \text{where} \quad \eta = -\varphi_{\mathrm{F}}(\omega_0)\frac{2B}{\omega_0}. \tag{61}$$

Substituting (61) into the integrand of (59), we obtain the following structure of the resulting imaging kernel matrix:

$$\mathbf{W} = e^{-2ik(R_{\boldsymbol{y}} - R_{\boldsymbol{z}})} \begin{pmatrix} V_0 & -V_1 & V_1 & -V_2 \\ V_1 & V_0 & V_2 & V_1 \\ -V_1 & V_2 & V_0 & -V_1 \\ -V_2 & -V_1 & V_1 & V_0 \end{pmatrix}. \tag{62}$$

The matrix entries are functions of two variables: $\xi = B(R_{\boldsymbol{y}} - R_{\boldsymbol{z}})/c$, cf. (12), and η defined in (61):

$$\begin{aligned} V_0 \equiv V_0(\xi;\eta) &= \int_{-\tau/2}^{\tau/2} e^{-2i\xi\tilde{t}/\tau} \cos^2(\Delta\varphi_{\mathrm{F}}) d\tilde{t} = \frac{\tau}{2}\big(\operatorname{sinc}\xi + F_0(\xi;\eta)\big), \\ V_1 \equiv V_1(\xi;\eta) &= \int_{-\tau/2}^{\tau/2} e^{-2i\xi\tilde{t}/\tau} \cos(\Delta\varphi_{\mathrm{F}}) \sin(\Delta\varphi_{\mathrm{F}}) d\tilde{t} = \frac{\tau}{2i} F_1(\xi;\eta), \\ V_2 \equiv V_2(\xi;\eta) &= \int_{-\tau/2}^{\tau/2} e^{-2i\xi\tilde{t}/\tau} \sin^2(\Delta\varphi_{\mathrm{F}}) d\tilde{t} = \frac{\tau}{2}\big(\operatorname{sinc}\xi - F_0(\xi;\eta)\big), \end{aligned} \tag{63}$$

where we have additionally introduced the notations:

$$F_0(\xi;\eta) = \frac{1}{\tau}\int_{-\tau/2}^{\tau/2} e^{-2i\xi\tilde{t}/\tau}\cos(2\eta\tilde{t}/\tau)\,d\tilde{t} = \frac{1}{2}\big(\operatorname{sinc}(\xi-\eta)+\operatorname{sinc}(\xi+\eta)\big),$$
$$F_1(\xi;\eta) = \frac{i}{\tau}\int_{-\tau/2}^{\tau/2} e^{-2i\xi\tilde{t}/\tau}\sin(2\eta\tilde{t}/\tau)\,d\tilde{t} = \frac{1}{2}\big(\operatorname{sinc}(\xi-\eta)-\operatorname{sinc}(\xi+\eta)\big). \tag{64}$$

It can be seen that as $\eta \to 0$ (or as $\varphi_{\mathrm{F}} \to 0$, see (61)), the matrices in (60) and (62) become diagonal, and the matrix imaging operator in (58) turns into a set of scalar imaging operators acting on individual reflectivity channels, see (13). The analytic expressions for L_2-norms of the matrix entries in (62) are given in [11]; for small η, they yield

$$\frac{\|V_1\|_2^2(\eta)}{\|V_0\|_2^2(\eta)} \approx \frac{\eta^2}{12}\,, \quad \frac{\|V_2\|_2^2(\eta)}{\|V_0\|_2^2(\eta)} \approx \frac{\eta^4}{80}\,, \tag{65}$$

where for a function $f(\xi;\eta)$, the norm is defined as

$$\|f\|_2^2(\eta) = \int_{-\infty}^{\infty} |f(\xi;\eta)|^2\,d\xi.$$

The asymptotic expressions (65) work well up to $|\eta| \lesssim 1$. We see that for this range of η, the leading off-diagonal terms are due to V_1. For $|\eta| \ll 1$,

$$F_0(\xi;\eta) \approx \frac{1}{\tau}V_0(\xi;\eta) \approx \operatorname{sinc}\xi, \quad F_1(\xi;\eta) = \frac{2i}{\tau}V_1(\xi;\tau) \approx -\eta\operatorname{sinc}'\xi, \tag{66}$$

see Fig. 3.

6 Polarimetric radar interferometry in the presence of dFR

6.1 Simplified polarimetric model for reconstruction of the parameters of vegetaton layer

In order to understand the mechanics of the effect of differential Faraday rotation (dFR) on the polarimetric radar interferometry (PolInSAR), we first build a simplified polarimetric model that still supports the major properties of polarimetric geophysical observations. Our analysis will focus on one of the most popular PolInSAR tasks, namely, reconstruction of parameters of the aboveground vegetation layer.

In the "random volume over ground" (RVoG) paradigm, see (33)–(35), we specify reflectivities of the two components of the model, namely, $\sigma_{\mathrm{g}}^2(\mathbf{w})$ (ground) and $\sigma_{\mathrm{v}}^2(\mathbf{w})$ (volume), for at least two polarizations (i.e., two different values of $\mathbf{w}$). From the asymptotic models of ground scattering supported by observations, we know that the ground contribution into the cross-polarized scattering is very small [36, 37, 28]. At the same time, ground reflectivity may dominate the radar return on HH-polarization; this is sometimes explained by the

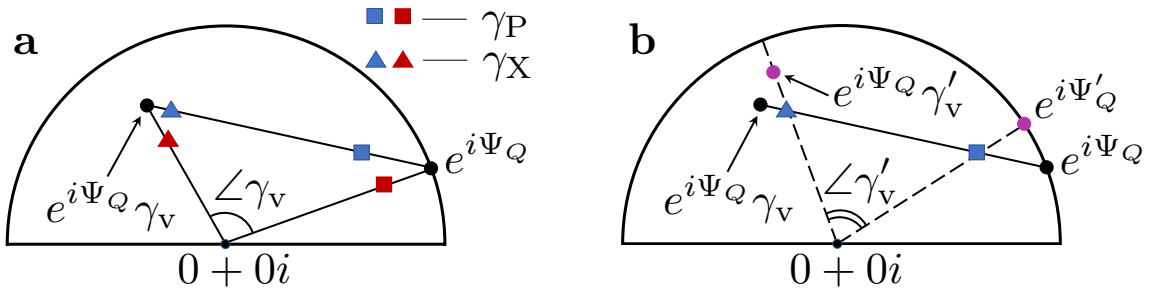

Figure 6: Coherence loci on a complex plane for the case $\mathcal{A} = 0$. (a) Blue markers: Scenario A (Section 6.2), red markers: Scenario B (Section 6.3). (b) Blue markers: same as in (a), purple markers: Scenario AB (Section 6.4).

ground-trunk double-bounce mechanism [7, 45]. For the foliage, the microscopic reflectivity models [28] yield comparable values for the co-polarized and cross-polarized channels; in our model, we will use a constant $\mathcal{A} \gtrsim 1$ to describe this ratio. Additionally, we assume that the reflectivities in different polarization channels don't correlate; although this assumption contradicts the observations showing high correlation between the co-polarized channels in the reflection from the ground (see, e.g., [26, 37]), we can still use it as long as we consider only one co-polarized channel. Accordingly, using the subscripts P and X for the co- and cross-polarized channels of our simplified polarimetric setup, respectively, we express reflectivity of the scatterer as follows:

$$\begin{aligned} \sigma^2_{\mathrm{P}}(h) &= \sigma^2_{\mathrm{g}}\delta(h-h_{\mathrm{g}}) + \mathcal{A}\sigma^2_{\mathrm{v}}\frac{1}{D}\chi_D(h-h_{\mathrm{g}}-h_{\mathrm{v}}), \\ \sigma^2_{\mathrm{X}}(h) &= \sigma^2_{\mathrm{v}}\frac{1}{D}\chi_D(h-h_{\mathrm{g}}-h_{\mathrm{v}}). \end{aligned} \tag{67}$$

It can be seen that (67) is a further simplification of model (34),(35); in particular, we assume that the coefficient $\mathcal{A}$ is known.

The off-diagonal entries of the imaging kernel (62) in the presence of dFR result in cross-talk between the polarimetric channels. This effect is controlled by the value of parameter $\eta = -\varphi_{\mathrm{F}}(\omega_0)\cdot 2B/\omega_0$, see (61). In the interferometric settings, due to the subband selection as in (21), we introduce

$$\tilde{\eta} = \eta \cdot \frac{\tilde{B}}{B}. \tag{68}$$

Another effect of the subband selection is the shift of the central frequencies of the frequency bands for the respective images. In order to avoid additional distortions, we choose

$$\varphi^{*(1)}_{\mathrm{F}} = \varphi_{\mathrm{F}}(\omega_1), \quad \varphi^{*(2)}_{\mathrm{F}} = \varphi_{\mathrm{F}}(\omega_2),$$

where ω_1 and ω_2 are defined via (21a), and use the resulting mean rotation angles for the corresponding intermediary images in (56) instead of φ^*_{F}, see (55).

Expressions for the interferometric coherences in the case of cross-talk due to the dFR can be obtained similarly to (41). We will expect $|\eta| < 1$ (thus, $|\tilde{\eta}| < 1$), see [11], and according to estimate (65), drop the terms due V_2 from the imaging kernel (62). Using the reflectivity model (67), imaging model (58) with noise contributions as in (45), definitions (20) and (37), and the aforementioned assumption about the absence of cross-channel correlation in the target reflectivity, we arrive at the following expressions for the complex interferograms $Q_{\mathrm{P}}, Q_{\mathrm{X}}$ and intensities $T_{\mathrm{P}}, T_{\mathrm{X}}$:

$$\begin{aligned} Q_{\mathrm{P}} &= e^{i\Psi_Q}\big(V_{Q0}(\sigma_{\mathrm{g}}^2 + \mathcal{A}\sigma_{\mathrm{v}}^2\gamma_{\mathrm{v}}) + 2V_{Q1}\sigma_{\mathrm{v}}^2\gamma_{\mathrm{v}}\big), \\ Q_{\mathrm{X}} &= e^{i\Psi_Q}\big(V_{Q0}\sigma_{\mathrm{v}}^2\gamma_{\mathrm{v}} + V_{Q1}(\sigma_{\mathrm{g}}^2 + \mathcal{A}\sigma_{\mathrm{v}}^2\gamma_{\mathrm{v}})\big), \\ T_{\mathrm{P}} &= V_{Q0}(\sigma_{\mathrm{g}}^2 + \mathcal{A}\sigma_{\mathrm{v}}^2) + 2V_{Q1}\sigma_{\mathrm{v}}^2 + \mathbf{N}^2, \\ T_{\mathrm{X}} &= V_{Q0}\sigma_{\mathrm{v}}^2 + V_{Q1}(\sigma_{\mathrm{g}}^2 + \mathcal{A}\sigma_{\mathrm{v}}^2) + \mathbf{N}^2, \end{aligned} \tag{69}$$

where (cf. (32))

$$\begin{aligned} V_{Q0} \equiv V_{Q0}(\eta) &= \int |V_0(\tilde{B}s\sin\theta/c;\tilde{\eta})|^2\, ds, \\ V_{Q1} \equiv V_{Q1}(\eta) &= \int |V_1(\tilde{B}s\sin\theta/c;\tilde{\eta})|^2\, ds, \end{aligned} \tag{70}$$

expressions for $V_0(\xi;\eta)$ and $V_1(\xi;\eta)$ are given in (63)–(66), and Ψ_Q is defined in (44). Note that similarly to (38), we assume in (69) that the intensities at the two antennas are the same and use T_{P} and T_{X} instead of $\sqrt{T_{\mathrm{P}}^{(1)}T_{\mathrm{P}}^{(2)}}$ and $\sqrt{T_{\mathrm{X}}^{(1)}T_{\mathrm{X}}^{(2)}}$, respectively. The coefficient 2 in the expressions for Q_{P} and T_{P} reflects the fact that the channel X is affected by a cross-talk from two cross-polarized channels, HV and VH, whereas the effect of the weaker co-polarized channel, i.e., VV, is ignored.

From (69), we can obtain expressions for interferometric coherences in the specified channels similarly to (39), and, additionally, the cross-channel intensity ratio:

$$\gamma_{\mathrm{P}} = \frac{Q_{\mathrm{P}}}{T_{\mathrm{P}}}, \quad \gamma_{\mathrm{X}} = \frac{Q_{\mathrm{X}}}{T_{\mathrm{X}}}, \quad M = \frac{T_{\mathrm{P}}}{T_{\mathrm{X}}}. \tag{71}$$

In (69), we consider $e^{i\Psi_Q}$ unknown, as discussed following (27); hence, determination of $e^{i\Psi_Q}$ is equivalent to the reconstruction of the local elevation. Other parameters to be reconstructed are the mean elevation h_{v} and thickness D of the vegetation layer. We will consider the left hand sides in (71) as the data for this inversion. Note that σ_{g}^2, σ_{v}^2, and $\mathbf{N}^2$ are also considered unknown, so there is generally not enough equations to perform the inversion.

A simple example of PolInSAR reconstruction can be obtained from a bare-bone model defined by

$$V_{Q1} = 0, \quad \mathbf{N}^2 = 0, \quad \text{and} \quad \mathcal{A} = 0. \tag{72}$$

These assumptions make the polarimetric channels decoupled and affected only by one component of the scatterer, namely, ground and foliage affect P- and X-channels, respectively. As a result, the first two expressions in (71) produce

$$\gamma_{\mathrm{P}} = e^{i\Psi_Q}, \quad \gamma_{\mathrm{X}} = e^{i\Psi_Q}\gamma_{\mathrm{v}}. \tag{73}$$

Relations (73) can be considered as the extreme cases of (43) for $m(\mathbf{w}) = \infty$ and $m(\mathbf{w}) = 0$, respectively. The reconstruction of the vegetation layer parameters from the data γ_{P} and γ_{X} in this case can be performed easily with the help of (41):

$$\Psi_Q = \angle\gamma_{\mathrm{P}}, \tag{74a}$$

$$h_{\mathrm{v}} = -\frac{1}{\kappa}\angle\gamma_{\mathrm{v}} = -\frac{1}{\kappa}(\angle\gamma_{\mathrm{X}} - \angle\gamma_{\mathrm{P}}), \tag{74b}$$

$$D = \frac{2}{\kappa}\operatorname{sinc}^{-1}|\gamma_{\mathrm{v}}| = \frac{2}{\kappa}\operatorname{sinc}^{-1}\left|\frac{\gamma_{\mathrm{X}}}{\gamma_{\mathrm{P}}}\right|, \tag{74c}$$

where $\operatorname{sinc}^{-1}(\zeta)$ is an inverse function to $\operatorname{sinc}\xi = \sin(\xi)/\xi$ for $0 \leqslant \zeta \leqslant 1$. Note that although the function $\operatorname{sinc}^{-1}(\zeta)$ can technically be defined on a wider interval, e.g., $\zeta_0 \leqslant \zeta \leqslant 1$, where $\zeta_0 = \min_\xi \operatorname{sinc}(\xi) \approx -0.2$, doing so for (74) creates ambiguity for reconstruction of h_{v} and D from complex-valued γ_{v}. We also see that h_{v} should not exceed the height ambiguity threshold specified in (29), and $D \leqslant h_{\mathrm{v}}/2$ by design, see Fig. 3.

Of course, reconstruction (74) cannot reveal any effect due to dFR because the latter requires a nonzero value of the parameter V_{Q1} entering (69). We will still try to avoid lifting all three assumptions in (72) simultaneously because this would make the setup too complicated for analytical treatment. Instead, we consider three scenarios that would simplify system (69) in different ways. The first scenario (see Section 6.2) permits dFR but not noise. The second scenario (see Section 6.3) permits noise but not dFR; this scenario also includes reconstruction of the parameters of vegetation layer. Finally, the third scenario (see Section 6.4) applies the first two in sequence; this way, it achieves the goal of this work by demonstrating the effect of dFR on PolInSAR reconstruction.

6.2 Scenario A: polarimetric interferometry with dFR and no noise: data only

Introduction of the parameter $\mathcal{A}$ in (67) allows us to redefine the ground-to-volume ratio m as a constant independent of polarization:

$$m = \frac{\sigma_{\mathrm{g}}^2}{\sigma_{\mathrm{v}}^2} = \text{const},$$

cf. (44). In addition, we introduce parameter q to characterize the magnitude of the dFR effect:

$$q = \frac{V_{Q1}}{V_{Q0}} \approx \frac{1}{12}\tilde{\eta}^2, \tag{75}$$

see (65), (68), and (70). Eventually, we remove the noise term by setting $\mathbf{N}^2 = 0$. Expressions in (71) take the following form:

$$\begin{aligned}
\gamma_{\mathrm{P}} &= e^{i\Psi_Q}\left(1 + \frac{\mathcal{A}+2q}{m+\mathcal{A}+2q}(\gamma_{\mathrm{v}} - 1)\right),\\
\gamma_{\mathrm{X}} &= e^{i\Psi_Q}\left(\gamma_{\mathrm{v}} + \frac{qm}{1+q(m+\mathcal{A})}(1-\gamma_{\mathrm{v}})\right),\\
M &= \frac{m+\mathcal{A}+2q}{1+q(m+\mathcal{A})}\,.
\end{aligned} \tag{76}$$

One can notice that the first two expressions in (76) resemble (43), i.e., they result in a complex value on a segment of straight line between $e^{i\Psi_Q}$ and $e^{i\Psi_Q}\gamma_{\rm v}$, see Figs. 4, 6a and formula (84). As compared to the primitive case of (73), the points $\gamma_{\rm P}$ and $\gamma_{\rm X}$ shift towards each other starting from points $e^{i\Phi_Q}$ and $e^{i\Phi_Q}\gamma_{\rm v}$, respectively. As a result, if we ignore the fact that $|\gamma_{\rm P}|<1$ and apply the reconstruction formulae (74a) and (74b) to the case illustrated in Fig. 6a, i.e., $0<\angle\gamma_{\rm v}<\pi$, we will obtain the ground elevation higher than actual and the value of $h_{\rm v}$ smaller than actual, see Fig. 6b. In the case of $-\pi<\angle\gamma_{\rm v}<0$, the reconstructed ground elevation becomes lower than actual, and $h_{\rm v}$ higher than actual.

6.3 Scenario B: polarimetric interferometry with noise and no dFR: data and inversion

Unlike in Section 6.2, we take $q=0$ but $\mathbf{N}^2>0$. Instead of using a polarization-dependent SNR as in (47), we will parametrize the noise term in (69) using

$$n_{\rm g}=\frac{\mathbf{N}^2}{V_{Q0}\sigma_{\rm g}^2}=\text{const}. \tag{77}$$

In this case, expressions in (71) lead to the following system:

$$\begin{aligned}\gamma_{\rm P}&=e^{i\Psi_Q}\frac{m+\gamma_{\rm v}\mathcal{A}}{m+\mathcal{A}+n_{\rm g}m},\\ \gamma_{\rm X}&=e^{i\Psi_Q}\frac{\gamma_{\rm v}}{1+n_{\rm g}m},\\ M&=\frac{m+\mathcal{A}+n_{\rm g}m}{1+n_{\rm g}m}\,.\end{aligned} \tag{78}$$

We can observe that the second equation in (78) is equivalent to (48), which is not surprising because in the absence of dFR, the X-channel is due entirely to the volume scatterer, see (67). So, the same useful visualization support works for this equation, namely, that on the complex plane, $\gamma_{\rm X}$ is located on a segment of straight line between the origin and $e^{i\Psi_Q}\gamma_{\rm v}$, see Fig. 4. By representing the first equation in (78) as

$$\gamma_{\rm P}=e^{i\Psi_Q}r_\gamma r_n,\quad \text{where}\quad r_\gamma=\Big(1+\frac{\mathcal{A}}{m+\mathcal{A}}(\gamma_{\rm v}-1)\Big),\quad r_n=\frac{m+\mathcal{A}}{m+\mathcal{A}+n_{\rm g}m},$$

we see that it combines the behaviors of the type (43) and (48): the complex point $e^{i\Psi_Q}$ is shifted towards $e^{i\Psi_Q}\gamma_{\rm v}$ due to the complex-valued factor r_γ, similarly to Scenario A, and then towards the origin due to the real-valued factor r_n. In a hypothetical case of $\mathcal{A}=0$ that yields $r_\gamma=1$, the first two equations in (78) are similar (note that $\gamma_{\rm g}=1$, see (41)), so the effect of noise can be described as a shift of points $\gamma_{\rm P}$ and $\gamma_{\rm X}$ from their "original" positions $e^{i\Psi_Q}$ and $e^{i\Psi_Q}\gamma_{\rm v}$, respectively, towards the origin, see Figs. 4 and 6a. Hence, for $\mathcal{A}=0$, the first two expressions in the primitive inversion procedure (74) remain valid even though $\mathbf{N}^2\neq 0$. Note that this behavior is not equivalent to the model of [46] where the noise was attributed to the temporal decorrelation and hence assigned to the response from the vegetation layer but not from the ground.

The inversion in this scenario is realized as follows. With the left hand side of (78) considered as data, we solve this system for the unknown $\gamma_{\rm v}$, Ψ_Q, m, and $n_{\rm g}$. As $\gamma_{\rm v}$, $\gamma_{\rm P}$, and $\gamma_{\rm X}$ are complex, the number of equations is equal to the number of unknowns. The key step in finding an analytic solution is eliminating $\gamma_{\rm v}$ from the first two equations and extracting $e^{i\Psi_Q}$:

$$e^{i\Psi_Q} = \left(1 + \frac{\mathcal{A}}{m} + n_{\rm g}\right)\left(\gamma_{\rm P} - \gamma_{\rm X}\frac{\mathcal{A}}{M}\right). \tag{79}$$

This leads to

$$1 + \frac{\mathcal{A}}{m} + n_{\rm g} = |\Gamma|^{-1}, \quad \text{where} \quad \Gamma = \gamma_{\rm P} - \gamma_{\rm X}\frac{\mathcal{A}}{M}.$$

The latter equation, together with the equation for M in (78), are solved for m and $n_{\rm g}$. Finally, from the equation for $\gamma_{\rm X}$ in (78) we obtain

$$\gamma_{\rm v} = \gamma_{\rm X}\frac{|\Gamma|}{\Gamma}\frac{1-\mathcal{A}}{M|\Gamma| + 1 - M}. \tag{80}$$

Formulae (79) and (80), via (44) and

$$h_{\rm v} = -\frac{1}{\kappa}\angle\gamma_{\rm v}, \quad D = \frac{2}{\kappa}\,\mathrm{sinc}^{-1}|\gamma_{\rm v}|, \tag{81}$$

cf. (74b) and (74c), provide inversion of the PolInSAR observables for the geophysical parameters of the vegetation-covered terrain in the absence of dFR. We should emphasize that this reconstruction is exact as long as the observables obey (78).

6.4 Scenario AB: effect of dFR on PolInSAR inversion

The key step of this entire work is to combine Scenarios A and B from Sections 6.2 and 6.3, respectively, in the following fashion. First, we assume certain values of q, $\gamma_{\rm v}$, Ψ_Q, and m, and generate the data according to Scenario A (see (76)) that has dFR but no noise. Note that we don't have to specify the value of $n_{\rm g}$ of (77) for Scenario A. As in Section 6.2, we obtain $|\gamma_{\rm P}| < 1$. In the absence of information about dFR, this decorrelation may be attributed to noise. Accordingly, we apply the inversion to the above data as in Scenario B (see (79)–(81)) that assumes noise but no dFR. The outputs of this procedure will be called Ψ'_Q and $\gamma'_{\rm v}$. In doing so, we may expect some errors: $\Psi'_Q \neq \Psi_Q$ and/or $\gamma'_{\rm v} \neq \gamma_{\rm v}$, because the exact reconstruction in Scenario B assumes $q = 0$. We will associate the effect of dFR on PolInSAR reconstruction with these errors and will use the magnitudes of these errors as a measure of the said effect.

For the case of $\mathcal{A} = 0$, this combined scenario can be conveniently illustrated on a complex plane as in Fig. 6b. For this case, it is easy to see that the errors in Ψ_Q and $h_{\rm v}$ will have the same signs as described in Section 6.2.

As formulations for the case $\mathcal{A} > 0$ are complicated for analytic treatment, we obtain quantitative characteristics of the reconstruction errors numerically. Fig. 7a illustrates the resulting errors of reconstruction of Ψ_Q; this characterizes the effect on the derived ground topography. Fig. 7b presents the reconstruction error for the complex coherence of the volume scatterer, while the effect on the elevation and thickness of the foliage layer is illustrated by Figs. 7c and 7d, respectively.

A more detailed analysis of these simulations is given in Section 7.

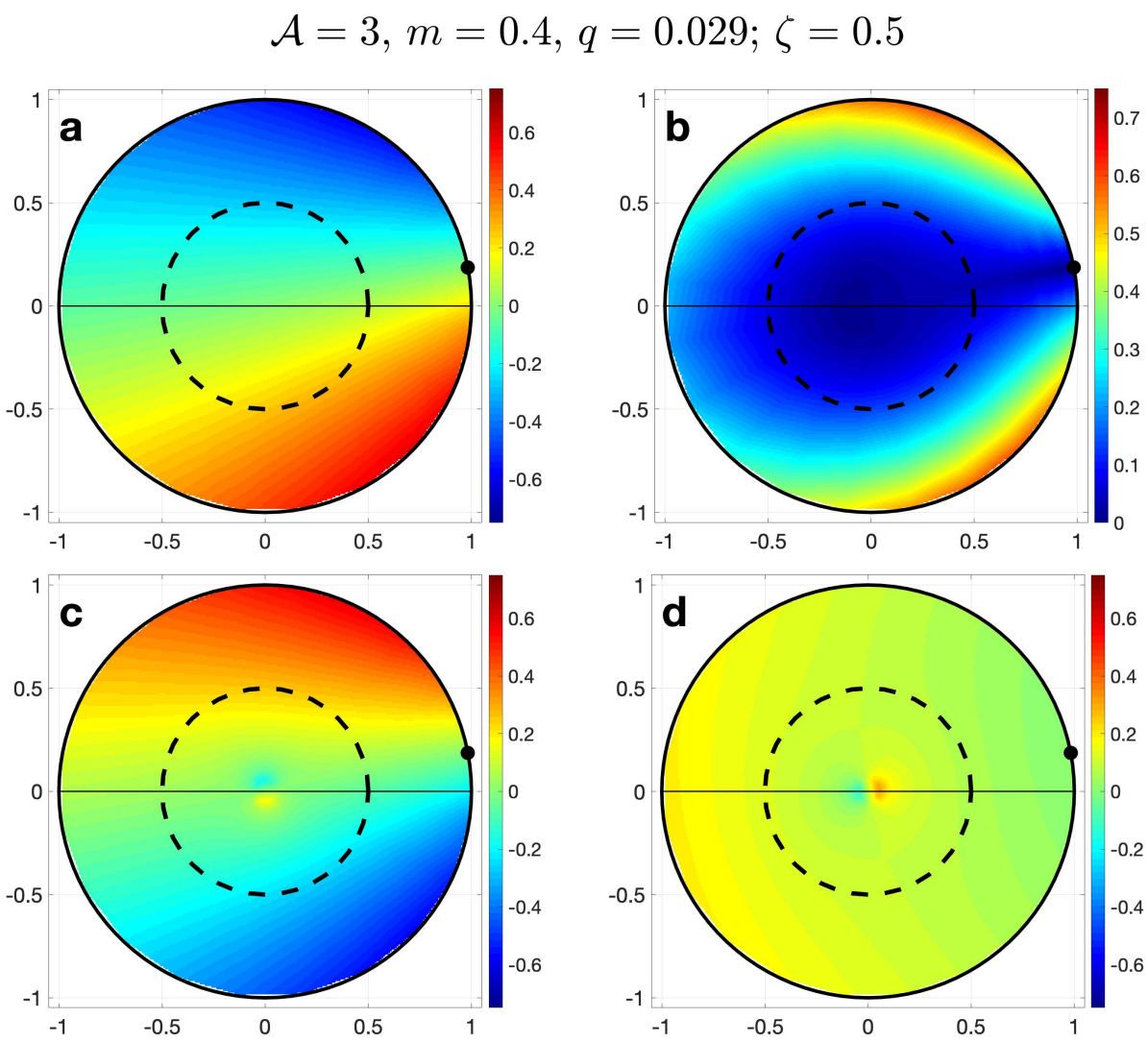

Figure 7: Reconstruction errors for Scenario AB, Section 6.4, as functions of $(\mathrm{Re}\,\gamma_\mathrm{v}, \mathrm{Im}\,\gamma_\mathrm{v})$. The true value of $e^{i\Psi_Q}$ is shown by a black dot. (a) $\Psi'_Q - \Psi_Q$; (b) $|\gamma'_\mathrm{v} - \gamma_\mathrm{v}|$; (c) $\angle\gamma'_\mathrm{v} - \angle\gamma_\mathrm{v}$; (d) $|\gamma'_\mathrm{v}/\gamma_\mathrm{v}| - 1$. The dashed circle corresponds to the threshold value ζ in (82).

7 Results

The scenario presented in Section 6.4 allows us to evaluate the effect of differential Faraday rotation (dFR) on the reconstruction of the foliage layer parameters in polarimetric radar interferometry. The manifestation of dFR can be observed in the systematic reconstruction errors of the ground topography and vegetation layer parameters, i.e., average layer elevation and thickness. The magnitude of the effect depends on several groups of parameters. One group includes the system parameters, such as carrier frequency and bandwidth, see (51),(61). Another group consists of the parameters of the ionosphere defining the Faraday rotation, such as the local magnetic field and electron concentration, see (51). Yet the third

group of parameters are related to the PolInSAR procedure; this group includes the polarimetric wavenumber κ (which, in turn, is defined by the interferometric angle $\Delta\theta$, see (25)) and parameters of the scatterer: Ψ_Q, $\gamma_{\rm v}$, m, $\mathcal{A}$, etc., see Sections 4 and 6.1. Eventually, these parameters are combined into the coefficients and variables of systems (76) and (78).

In particular, we take the ionospheric and imaging parameters as in [11], namely, the total electron content of $50\,TECU$, $|\boldsymbol{H}^{(0)}| = 0.5\,Gs$, and parallel propagation. For interferometry, we set $\tilde{B}/B = 0.85$; substituting this into (21b) and (29), we obtain $\Delta\theta \approx 0.007 rad$ and ambiguity height about $60m$, respectively. In the plots that follow, we let one or more scatterer parameters vary.

Fig. 7 plots reconstruction errors for Scenario AB, Section 6.4, as functions of $\gamma_{\rm v}$. The error metrics plotted in panels a, c, and d are chosen to correspond to the geometric characteristics of the scatterer, see Section 6.4. However, the last two of these metrics have anomalies in the vicinity of the origin, whereas the underlying error in the complex coherence (panel b) has no such irregularities. From the inversion formulae (81) (see also Fig. 6b), we determine that the errors can be especially high when the value of $|\gamma_{\rm X}|$ resulting from (76) is small. We exclude this anomalous behavior by setting a threshold $\zeta = 0.5$ on the value of $|\gamma_{\rm v}|$ when calculating an error metric; note that this is also helpful in view of possible ambiguity of inversion of the function $\mathrm{sinc}(\xi)$, see the note following (74). In particular, if $f(\alpha, \gamma_{\rm v})$ is any of the error metrics shown in Fig. 7 and α denotes any parameter other than $\gamma_{\rm v}$, then we use the threshold in the following definition of the error function f_α:

$$f_\alpha(\alpha;\zeta) = \max_{\zeta\leqslant|\gamma_{\rm v}|\leqslant 1} |f(\alpha,\gamma_{\rm v})|. \tag{82}$$

The value of ζ corresponds to the radius of the dashed circles in Fig. 7.

In Fig. 8, we present the dependence of reconstruction errors on parameter q of (75) that defines the magnitude of the dFR effect, for two different values of parameter $\mathcal{A}$. These errors are defined according to (82) and characterize reconstruction of parameters Ψ_Q, $h_{\rm v}$, and D in Scenario AB. Additionally, we indicate the values of q for three satellite-based radar systems considered in the literature [11, 13, 47], with the ionospheric parameters as in [11]. An arbitrarily chosen error threshold of 0.3 (or 30%) is also shown on the plots; errors above this level can be considered as significant for most applications. Additional error plots for the values of q corresponding to the BIOMASS satellite are given in Fig. 9. We see that in most cases, the error level is below the chosen threshold.

8 Discussion

The goal of this article is to introduce the differential Faraday rotation into the context of polarimetric radar interferometry. The reflectivity and data collection models presented by equations (67) and (69), respectively, are specifically designed for this purpose. Although they exhibit many features of the standard RVoG model [28] that is used to reconstruct properties of vegetation layer from PolInSAR observations, they also have incorporated multiple simplifications that may compromise inversion if applied to real data. As an example, we can consider a case where the dependence of foliage reflectivity on polarization, characterized by the value of parameter $\mathcal{A}$ in (67), is known with some error. The effect of this ambiguity may be explored in the following scenario.

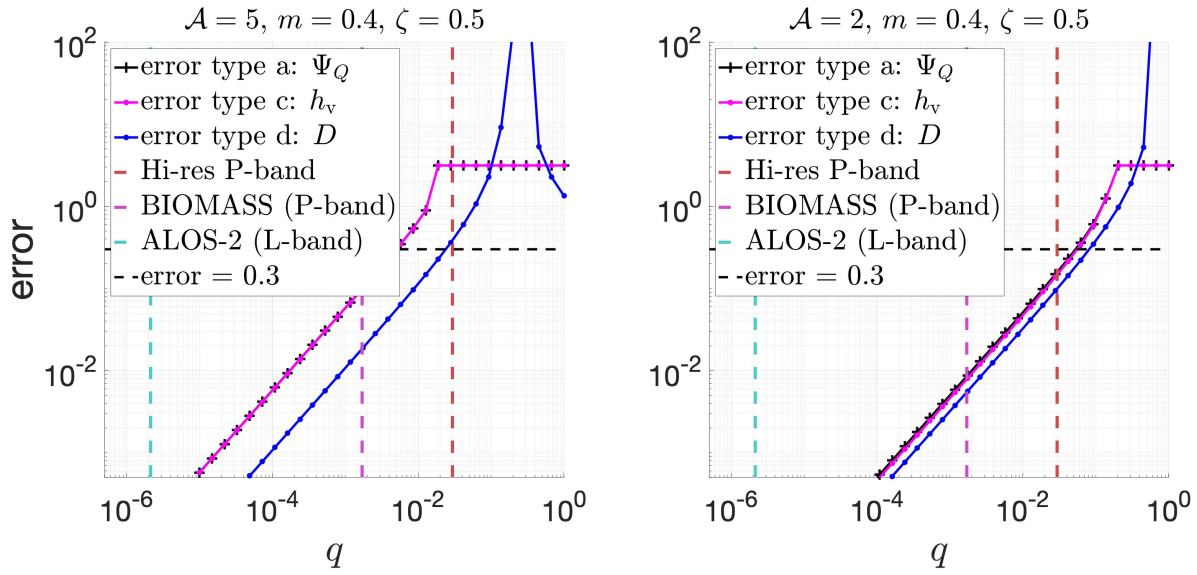

Figure 8: Reconstruction errors in Scenario AB vs. the level of dFR effect defined in (75) for two different values of parameter $\mathcal{A}$, see (67). In each plot, three colored curves are built according to (82) for the error metrics displayed in panels a, c, and d of Fig. 7 and representing reconstruction of parameters Ψ_Q, h_v, and D, respectively. The dashed vertical line called "Hi-res P-band" corresponds to the system described in [11]; for parameters of the BIOMASS and ALOS-2 systems see [13] and [47], respectively.

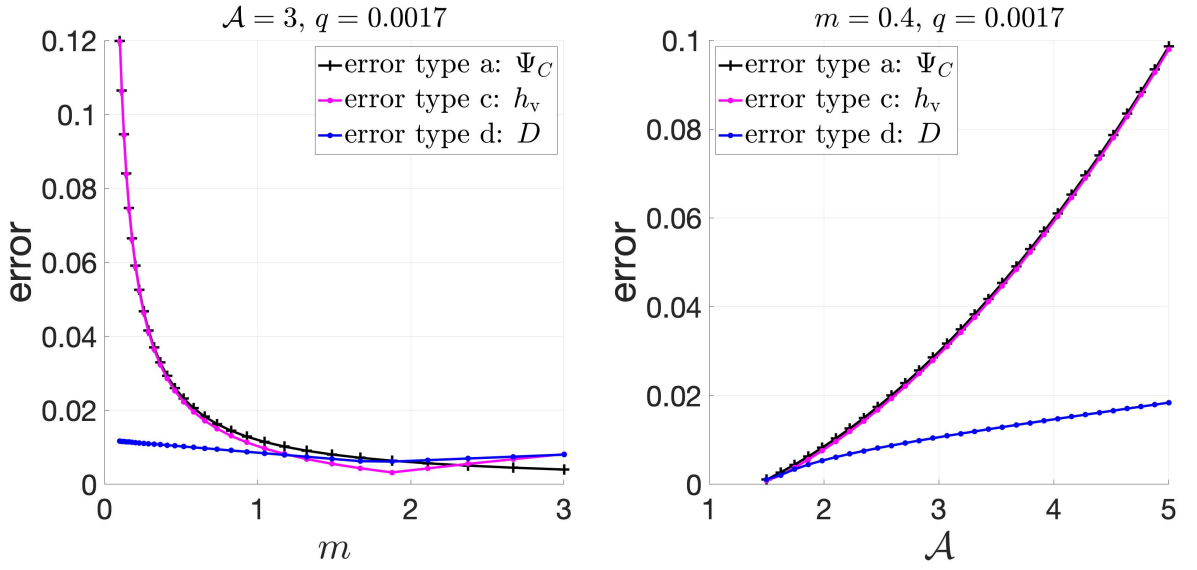

Figure 9: Dependence of reconstruction errors in Scenario AB defined similarly to Fig. 8 on m (left panel) and $\mathcal{A}$ (right panel). The value of q corresponds to the BIOMASS system in Fig. 8.

Scenario C: Step 1: Data is generated as in Scenario B, see (78), with $\mathcal{A} = \mathcal{A}_{\text{in}}$.

Step 2: Inversion is performed as in Scenario B, see (79),(80), but with $\mathcal{A} = \mathcal{A}_{\text{out}} \neq \mathcal{A}_{\text{in}}$. (83)

We define reconstruction errors due to Scenario C in a way similar to Scenario AB, see Sections 6.4 and 7. Fig. 10 illustrates these errors for the case where the values of $\mathcal{A}_{\rm in}$ and $\mathcal{A}_{\rm out}$ differ by about 8%. We see that the level of errors in this case is comparable to that presented in Fig. 7. Note that the actual reflectivity measurements from SAR are subject to speckle [26], and the foliage level is itself highly irregular, so even if separate measurements of $\mathcal{A}$ were available, achieving the accuracy of 10% or better cannot be guaranteed. A more realistic option is to consider the value of $\mathcal{A}$ unknown and increase the amount of data by including data from additional polarizations; however, this would make the analysis of the inversion less transparent.

Other possible flaws of the model may include the following.

- Throwing away one of the two co-polarized channels, namely, VV, in (69).
- Additive noise terms in model (69). In real settings, at least for the case where the two images are acquired at different times, we should expect much bigger decorrelation of the foliage scatterer because it can change its shape due to a change of local weather. A more appropriate model describing this effect can be found in [46].
- The reconstructed value of $\gamma_{\rm v}$ vanishes as $\mathcal{A} \to 1$, see (80). While the case of $\gamma_{\rm v} = 0$ is quite legitimate in the adopted model, see (41), it results in large errors in the complex argument of $\gamma_{\rm v}$ and, eventually, in $h_{\rm v}$ via (81).

Despite these deficiencies, we still consider model (69) acceptable for the parameters used to create Figs. 7–9, and the obtained results reliable up to the order of magnitude.

9 Conclusion

For satellite-based Earth-observing radars, differential Faraday rotation explained in Section 5 introduces systematic errors into the parameters of the vegetation layer reconstructed using the polarimetric radar interferometry (PolInSAR) approach. The magnitude of errors depends on the parameters of the radar system and the state of ionosphere. Using a simplified polarimetric scatterer and imaging model, we have shown that for the existing X-, C-, and L-band space-based systems, as well as for the planned P-band BIOMASS system, these errors can be ignored, as demonstrated by Figs. 8 and 9. However, for future systems that may combine even lower frequencies with high bandwidth, this result has to be re-evaluated using a more representative model, and approaches to mitigation of these errors should be analyzed.

A Coherence on a complex plane

Consider a pair of random complex variables, a_1 and a_2, with $\langle|a_1|^2\rangle = \langle|a_2|^2\rangle = a^2$, where a is real. Take another such pair, b_1 and b_2, with $\langle|b_1|^2\rangle = \langle|b_2|^2\rangle = b^2$. The coherence within the pairs is defined by

$$\gamma_a = \frac{\langle \overline{a_1} a_2 \rangle}{\big(\langle|a_1|^2\rangle\langle|a_2|^2\rangle\big)^{1/2}} = \frac{\langle \overline{a_1} a_2 \rangle}{a^2}, \quad \gamma_b = \frac{\langle \overline{b_1} b_2 \rangle}{\big(\langle|b_1|^2\rangle\langle|b_2|^2\rangle\big)^{1/2}} = \frac{\langle \overline{b_1} b_2 \rangle}{b^2}.$$

$\mathcal{A}_{\rm in} = 3,\ \mathcal{A}_{\rm out} = 3.25,\ m = 0.4,\ n_{\rm g} = 0.15;\ \zeta = 0.5$

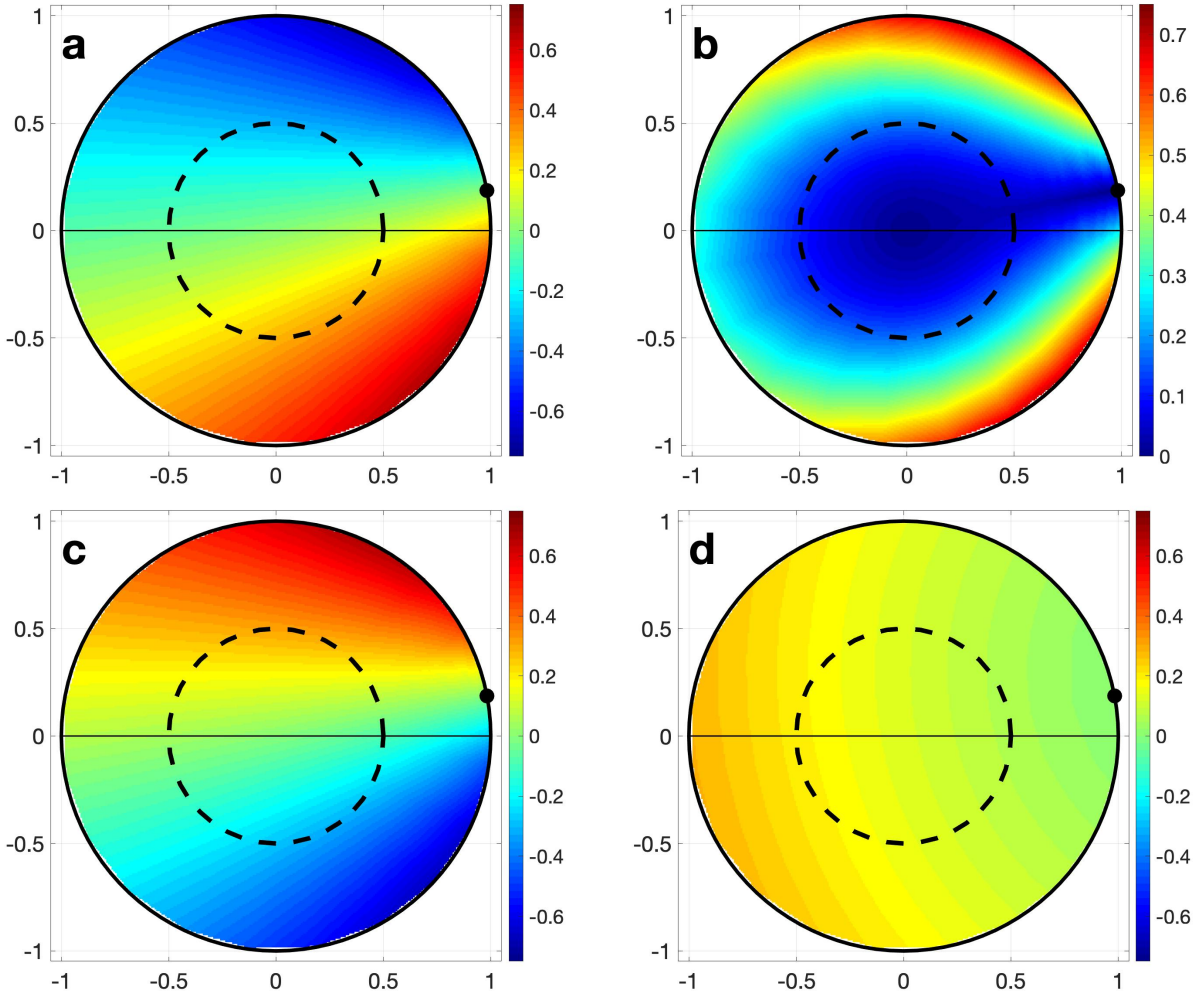

Figure 10: Same as in Fig. 7, but for Scenario C, see (83).

Suppose that there is no correlation between the pairs:

$$\langle \overline{a_1} b_1 \rangle = \langle \overline{a_1} b_2 \rangle = \langle \overline{a_2} b_1 \rangle = \langle \overline{a_2} b_2 \rangle = 0,$$

and consider the sums $c_1 = a_1 + b_1$ and $c_2 = a_2 + b_2$. The coherence between c_1 and c_2 will be given by

$$\gamma_c = \frac{\big\langle \overline{(a_1 + b_1)}(a_2 + b_2) \big\rangle}{\big(\langle |a_1 + b_1|^2 \rangle \langle |a_2 + b_2|^2 \rangle \big)^{1/2}} = \frac{\langle \overline{a_1} a_2 \rangle + \langle \overline{b_1} b_2 \rangle}{a^2 + b^2} = \gamma_a \frac{a^2}{a^2 + b^2} + \gamma_b \frac{b^2}{a^2 + b^2}. \tag{84}$$

Relation (84) shows that on a complex plane, γ_c is located on a segment of a straight line connecting points γ_a and γ_b.

In the context of Section 4, we can associate c_1 and c_2 with $\mathcal{I}(\boldsymbol{y}; \boldsymbol{x}^{(1)}, \ldots)$ and $\mathcal{I}(\boldsymbol{y}; \boldsymbol{x}^{(2)}, \ldots)$, respectively, see (20) and (36), a_1 and a_2 with the contributions to these images due to the ground, i.e., $\mathcal{I}_{\mathrm{Gr}}$, and b_1 and b_2 with the contributions due to the volume $\mathcal{I}_{\mathrm{Vol}}$. Accordingly, equation (84) corresponds to (42).

References

[1] Richard Bamler and Philipp Hartl. Synthetic aperture radar interferometry. *Inverse problems*, 14(4):R1, 1998. 2, 6

[2] Paul A. Rosen, Scott Hensley, Ian R. Joughin, Fuk K. Li, Søren N. Madsen, Ernesto Rodriguez, and Richard M. Goldstein. Synthetic aperture radar interferometry. *Proceedings of the IEEE*, 88(3):333–382, 2000. 2, 6, 10

[3] Margaret Cheney and Brett Borden. *Fundamentals of Radar Imaging*, volume 79 of *CBMS-NSF Regional Conference Series in Applied Mathematics*. SIAM, Philadelphia, 2009. 2, 5

[4] Tom G Farr, Paul A Rosen, Edward Caro, Robert Crippen, Riley Duren, Scott Hensley, Michael Kobrick, Mimi Paller, Ernesto Rodriguez, Ladislav Roth, et al. The shuttle radar topography mission. *Reviews of geophysics*, 45(2), 2007. 2

[5] Gerhard Krieger, Alberto Moreira, Hauke Fiedler, Irena Hajnsek, Marian Werner, Marwan Younis, and Manfred Zink. TanDEM-X: A satellite formation for high-resolution SAR interferometry. *IEEE Transactions on Geoscience and Remote Sensing*, 45(11):3317–3341, 2007. 2

[6] Mikhail Gilman and Semyon Tsynkov. A mathematical perspective on radar interferometry. *Inverse Problems & Imaging*, 2020. Submitted for publication. 2, 7, 8, 9, 10

[7] Andreas Reigber and Alberto Moreira. First demonstration of airborne SAR tomography using multibaseline L-band data. *IEEE Transactions on Geoscience and Remote Sensing*, 38(5):2142–2152, 2000. 2, 19

[8] Shane R Cloude and Konstantinos P Papathanassiou. Polarimetric SAR interferometry. *IEEE Transactions on Geoscience and Remote Sensing*, 36(5):1551–1565, 1998. 2

[9] Konstantinos P. Papathanassiou and Shane R. Cloude. Single-baseline polarimetric SAR interferometry. *IEEE Transactions on Geoscience and Remote Sensing*, 39(11):2352–2363, 2001. 2, 12

[10] Gerhard Krieger, Konstantinos Panagiotis Papathanassiou, and Shane R Cloude. Spaceborne polarimetric SAR interferometry: Performance analysis and mission concepts. *EURASIP Journal on Advances in Signal Processing*, 2005(20):354018, 2005. 2, 13

[11] Mikhail Gilman and Semyon Tsynkov. Differential Faraday Rotation and Polarimetric SAR. *SIAM J. Appl. Math.*, 78(3):1422–1449, 2018. 2, 3, 14, 16, 17, 18, 20, 25, 26

[12] L. Li, Y. Zhang, Z. Dong, and D. Liang. Ionospheric polarimetric dispersion effect on low-frequency spaceborne SAR imaging. *IEEE Geoscience and Remote Sensing Letters*, 11(12):2163–2167, Dec 2014. 2

[13] T. Le Toan, S. Quegan, M. W. J. Davidson, Heiko Balzter, Ph. Paillou, K. Papathanassiou, S. Plummer, F. Rocca, S. Saatchi, H. Shugart, et al. The BIOMASS mission: Mapping global forest biomass to better understand the terrestrial carbon cycle. *Remote sensing of environment*, 115(11):2850–2860, 2011. 2, 25, 26

[14] Florence Heliere, Franco Fois, Marco Arcioni, Paolo Bensi, Michael Fehringer, and Klaus Scipal. Biomass P-band SAR interferometric mission selected as 7th Earth Explorer Mission. In *EUSAR 2014; 10th European Conference on Synthetic Aperture Radar; Proceedings of*, pages 1–4. VDE, 2014. 2

[15] Patricia A. Wright, Shaun Quegan, Nigel S. Wheadon, and C. David Hall. Faraday rotation effects on L-band spaceborne SAR data. *IEEE Transactions on Geoscience and Remote Sensing*, 41(12):2735–2744, 2003. 2

[16] F. J. Meyer and J. B. Nicoll. Prediction, detection, and correction of Faraday rotation in full-polarimetric L-band SAR data. *IEEE Transactions on Geoscience and Remote Sensing*, 46(10):3076–3086, October 2008. 2

[17] K. Davies and E. K. Smith. Ionospheric effects on satellite land mobile systems. *IEEE Antennas and Propagation Magazine*, 44(6):24–31, December 2002. 2

[18] Xiaoqing Pi, Anthony Freeman, Bruce Chapman, Paul Rosen, and Zhenhong Li. Imaging ionospheric inhomogeneities using spaceborne synthetic aperture radar. *J. Geophys. Res.*, 116(A4):1–13, April 2011. 2

[19] William B. Gail. Effect of Faraday rotation on polarimetric SAR. *IEEE Transaction on Aerospace and Electronic Systems*, 34(1):301–308, January 1998. 2

[20] Akira Ishimaru, Yasuo Kuga, Jun Liu, Yunjin Kim, and Tony Freeman. Ionospheric effects on synthetic aperture radar at 100MHz to 2GHz. *Radio Science*, 34(1):257–268, January-February 1999. 2

[21] F. J. Meyer. Performance requirements for ionospheric correction of low-frequency SAR data. *IEEE Transactions on Geoscience and Remote Sensing*, 49(10):3694–3702, October 2011. 2

[22] Michael Jehle, Othmar Frey, David Small, and Erich Meier. Measurement of ionospheric TEC in spaceborne SAR data. *IEEE Transactions on Geoscience and Remote Sensing*, 48(6):2460–2468, June 2010. 2

[23] M. Gilman and S. Tsynkov. Cross-channel contamination of PolSAR images due to frequency dependence of Faraday rotation angle. In *2018 IEEE Conference on Antenna Measurements Applications (CAMA), Västerås, Sweden*, pages 1–4. IEEE, Sept 2018. 2

[24] Jinhui Li, Yifei Ji, Yongsheng Zhang, Qilei Zhang, and Zhen Dong. Effects of ionosphere polarimetric dispersion on lower-frequency spaceborne SAR. In *2018 IEEE 3rd International Conference on Signal and Image Processing (ICSIP)*, pages 510–515. IEEE, 2018. 2

[25] Mikhail Gilman, Erick Smith, and Semyon Tsynkov. *Transionospheric synthetic aperture imaging*. Applied and Numerical Harmonic Analysis. Birkhäuser/Springer, Cham, Switzerland, 2017. 4, 5

[26] Chris Oliver and Shaun Quegan. *Understanding Synthetic Aperture Radar Images*. Artech House Remote Sensing Library. Artech House, Boston, 1998. 6, 19, 27

[27] Barbara Zitová and Jan Flusser. Image registration methods: A survey. *Image and Vision Computing*, 21(11):977–1000, 2003. 8

[28] Shane Cloude. *Polarisation: applications in remote sensing*. Oxford University Press, 2010. 9, 13, 14, 18, 19, 25

[29] H.A. Zebker and J. Villasenor. Decorrelation in interferometric radar echoes. *IEEE Transactions on Geoscience and Remote Sensing*, 30(5):950–959, September 1992. 9

[30] Alberto Moreira, Pau Prats-Iraola, Marwan Younis, Gerhard Krieger, Irena Hajnsek, and Konstantinos P. Papathanassiou. A tutorial on synthetic aperture radar. *IEEE Geoscience and Remote Sensing Magazine*, 1(1):6–43, 2013. 9

[31] Ramon F Hanssen. *Radar interferometry: data interpretation and error analysis*, volume 2 of *Remote Sensing and Digital Image Processing*. Kluwer Academic Publishers, New York, 2001. 9

[32] Giorgio Franceschetti and Riccardo Lanari. *Synthetic Aperture Radar Processing*. Electronic Engineering Systems Series. CRC Press, Boca Raton, FL, 1999. 9

[33] Didier Massonnet and Jean-Claude Souyris. *Imaging with Synthetic Aperture Radar*. Engineering Sciences: Electrical Engineering. EFPL Press. Distributed by CRC Press, Lausanne, Switzerland, 2008. 9, 12

[34] Charles V. Jakowatz, Jr., Daniel E. Wahl, Paul H. Eichel, Dennis C. Ghiglia, and Paul A. Thompson. *Spotlight-Mode Synthetic Aperture Radar: A Signal Processing Approach*. Springer, 1996. 9

[35] SR Cloude and KP Papathanassiou. Three-stage inversion process for polarimetric SAR interferometry. *IEE Proceedings-Radar, Sonar and Navigation*, 150(3):125–134, 2003. 13

[36] Alexander Voronovich. *Wave Scattering from Rough Surfaces*. Springer, Berlin, 1999. 14, 18

[37] Dayalan Kasilingam, Dale Schuler, and Jong-Sen Lee. The depolarization of radar backscatter from rough surfaces due to surface roughness and slopes. In *IGARSS 2001. Scanning the Present and Resolving the Future. Proceedings. IEEE 2001 International Geoscience and Remote Sensing Symposium (Cat. No. 01CH37217)*, volume 2, pages 925–927. IEEE, 2001. 14, 18, 19

[38] Jong-Sen Lee and Eric Pottier. *Polarimetric Radar Imaging from Basics to Applications*. Optical Science and Engineering. CRC Press, Boca Raton, 2009. 14

[39] Fawwaz T Ulaby and Charles Elachi. *Radar polarimetry for geoscience applications*. The Artech House Remote Sensing Library. Artech House, Inc., Norwood, MA, 1990. 14

[40] Max Born and Emil Wolf. *Principles of optics: Electromagnetic theory of propagation, interference and diffraction of light*. With contributions by A. B. Bhatia, P. C. Clemmow, D. Gabor, A. R. Stokes, A. M. Taylor, P. A. Wayman and W. L. Wilcock. Seventh (expanded) edition. Cambridge University Press, Cambridge, 1999. 14

[41] Julius Adams Stratton. *Eelctromagentic Theory*. McGraw-Hill Book Company, New York and London, 1941. 14

[42] V. L. Ginzburg. *The Propagation of Electromagnetic Waves in Plasmas*, volume 7 of *International Series of Monographs on Electromagnetic Waves*. Pergamon Press, Oxford, 1964. 14, 15

[43] Donald Gary Swanson. *Plasma Waves, 2nd Edition (Series in Plasma Physics and Fluid Dynamics)*. IOP Publishing, London, 2003. 15

[44] Mikhail Gilman, Erick Smith, and Semyon Tsynkov. Reduction of ionospheric distortions for spaceborne synthetic aperture radar with the help of image registration. *Inverse Problems*, 29(5):054005 (35pp), May 2013. 16

[45] Guillaume Brigot, Marc Simard, Elise Colin-Koeniguer, and Alexandre Boulch. Retrieval of forest vertical structure from PolInSAR data by machine learning using LIDAR-derived features. *Remote Sensing*, 11(4):381, 2019. 19

[46] KP Papathanassiou and Shane R Cloude. The effect of temporal decorrelation on the inversion of forest parameters from Pol-InSAR data. In *International Geoscience and Remote Sensing Symposium*, volume 3, pages III–1429, 2003. 22, 27

[47] Yukihiro Kankaku, Shinichi Suzuki, and Yuji Osawa. ALOS-2 mission and development status. In *2013 IEEE International Geoscience and Remote Sensing Symposium-IGARSS*, pages 2396–2399. IEEE, 2013. 25, 26